

Subarcsecond Submillimeter Imaging of the Ultracompact HII Region G5.89-0.39

T.R. Hunter¹, C.L. Brogan¹, R. Indebetouw^{1,2}, C.J. Cyganowski³

thunter@nrao.edu

cbrogan@nrao.edu

remy@virginia.edu

ccyganow@astro.wisc.edu

ABSTRACT

We present the first subarcsecond submillimeter images of the enigmatic ultracompact HII region (UCHII) G5.89-0.39. Observed with the SMA, the 875 μm continuum emission exhibits a shell-like morphology similar to longer wavelengths. By using images with comparable angular resolution at five frequencies obtained from the VLA archive and CARMA, we have removed the free-free component from the 875 μm image. We find five sources of dust emission: two compact warm objects (SMA1 and SMA2) along the periphery of the shell, and three additional regions further out. There is no dust emission inside the shell, supporting the picture of a dust-free cavity surrounded by high density gas. At subarcsecond resolution, most of the molecular gas tracers encircle the UCHII region and appear to constrain its expansion. We also find G5.89-0.39 to be almost completely lacking in organic molecular line emission. The dust cores SMA1 and SMA2 exhibit compact spatial peaks in optically-thin gas tracers (e.g. $^{34}\text{SO}_2$), while SMA1 also coincides with 11.9 μm emission. In CO(3-2), we find a high-velocity north/south bipolar outflow centered on SMA1, aligned with infrared H_2 knots, and responsible for much of the maser activity. We conclude that SMA1 is an embedded intermediate mass protostar with an estimated luminosity of 3000 L_\odot and a circumstellar mass of $\approx 1 M_\odot$. Finally, we have discovered an NH_3 (3,3) maser 12'' northwest of the UCHII region, coincident with a 44 GHz

¹NRAO, 520 Edgemont Rd, Charlottesville, VA, 22903

²University of Virginia, Astronomy Dept., P.O. Box 3818, Charlottesville, VA, 22903-0818

³University of Wisconsin, Madison, WI 53706

CH₃OH maser, and possibly associated with the Br γ outflow source identified by Puga et al. (2006).

Subject headings: HII regions — stars: formation — infrared: stars — ISM: individual (W28 A2) — ISM: individual (G5.89-0.39) — ISM: individual (IRAS 17574-2403) — techniques: interferometric — submillimeter

1. Introduction

The formation of massive stars is a fundamental process in astrophysics that is not well understood. The identification of ultracompact HII regions (UCHIIs) by Wood & Churchwell (1989) provided an important step forward in the study of massive star formation. These objects are less than 10^{17} cm in diameter, have a centimeter wavelength spectral index consistent with free-free emission, and are associated with far-infrared and submillimeter sources of high bolometric luminosity (Hunter et al. 2000; Thompson et al. 2006). Based on these characteristics, UCHIIs are believed to be ionized nebulae powered by young OB stars located at (or near) their centers and surrounded by high column densities of dust and molecular gas (Churchwell 2002). However, because of the high extinction at optical and infrared wavelengths, the exciting star is often too deeply embedded for its photospheric emission to be observed. In fact, until recently the exciting stars had been identified for only a few percent of UCHII regions (Hanson et al. 2002), with the first (and perhaps best) example being G29.96-0.02 (Watson et al. 1997; Martín-Hernández et al. 2003). Recent infrared studies have identified candidate ionizing sources toward several more UCHIIs (Alvarez et al. 2004; Apai et al. 2005; Comerón et al. 2006; Bik et al. 2006).

One UCHII for which a candidate ionizing star has been proposed is W28 A2, also known as G5.89-0.39, which is a well-known shell-type UCHII. Feldt et al. (2003) have identified a near-infrared star located along the northeastern rim of the radio shell which they argue is of spectral type O5 or earlier (hereafter called Feldt’s star). G5.89-0.39 is associated with a strong bipolar molecular outflow originally identified in CO by Harvey & Forveille (1988) and having one of the largest mass outflow rates known (Churchwell 1997). The outflow emission has been subsequently studied using single-dish CO and SiO (Klaassen et al. 2006; Choi et al. 1993; Acord et al. 1997) and interferometric CO, HCO⁺ (Watson et al. 2007) and SiO (Acord et al. 1997; Sollins et al. 2004) observations. The reported position angle of the outflow is notably different between the tracers, being nearly east-west in CO and HCO⁺ (position angle +84°), vs. northeast-southwest in SiO (position angle +30°). While masers of many kinds are seen toward and around G5.89-0.39 (the most recent images being: Hofner & Churchwell (1996) (H₂O), Stark et al. (2007) and Fish et al. (2005) (OH), and

Kurtz et al. (2004) (Class I CH₃OH)), the spatial-velocity gradients seen do not lead to a clear consensus view on the origin of the outflow. Furthermore, despite the fact that the purported O5 star lies along the axis of the SiO velocity gradient, it does not reside midway between the red and blue peaks, nor does it reside at the center of the radio shell. Such an asymmetry of the powering star’s location with respect to the radio shell was predicted by Ball et al. (1992) in their attempt to reconcile the mid-infrared and radio morphologies. Their model predicts the presence of dense molecular gas close to the northeast edge of the UCHII. While single-dish mm/submm surveys have established that G5.89-0.39 is a molecular line-rich source in the 875 μ m window (Hatchell et al. 1998), the majority of the lines are from sulfur-bearing species rather than the heavy organic molecules more typically seen in hot cores (Thompson & MacDonald 1999). Clearly, higher angular resolution studies of molecular gas and dust are required to test the various hypotheses on the nature of this complex massive star formation region and attempt to unify the observed phenomena.

Toward this end, we have obtained the first subarcsecond submillimeter (875 μ m) observations of G5.89-0.39. Our Submillimeter Array (SMA) images have a factor of seven higher angular resolution (in beam area) than the 1.4 mm Sollins et al. (2004) data, and are substantially more sensitive to dust emission and molecular lines. We interpret our unprecedented submillimeter images in the context of new images with comparable resolution constructed from the best available centimeter wavelength data in the VLA archive, 3 mm data from the new B-configuration of the Combined Array for Millimeter Astronomy (CARMA), and archival near- to mid-infrared data.

The distance to G5.89-0.39 used in the literature varies, although all papers agree that the source does not lie at the far kinematic distance. Acord et al. (1998) report a detection of the expansion of the nebula (though with a fairly low signal-to-noise of 2.5 ± 0.5 mas yr^{−1}) in multiepoch VLA images, which implies a distance of $2.0^{+0.7}_{-0.4}$ kpc. The kinematic distance based on the main-line OH maser velocity of $+18$ km s^{−1} is $3.8^{+1.0}_{-1.7}$ kpc (Fish et al. 2003). The kinematic distance based on the $+9.3$ km s^{−1} LSR velocity of CS(2-1) (Bronfman et al. 1996) is 2.6 kpc, while the distance to the nearby W28 supernova remnant is 1.9 kpc (Velázquez et al. 2002). We will adopt a distance of 2.0 kpc in this paper.

2. Observations

2.1. Submillimeter Array (SMA)

The SMA¹ observations were made with eight antennas in the extended configuration on 2006 June 05. Sky conditions were clear and the 225 GHz opacity measured by the tipping radiometer at the Caltech Submillimeter Observatory (CSO) varied from 0.065 to 0.081 during the observations. The SMA receivers have double sideband mixers with 2 GHz bandwidth centered at an intermediate frequency of 5 GHz. The front-end local oscillator was tuned to place the SiO(8-7) spectral line ($\nu = 347.33063$ GHz) in the center of correlator chunk 23 in the upper sideband (USB), resulting in center frequencies of 336.46 GHz in lower sideband (LSB) and 346.46 GHz in USB. The data were taken with a channel width of 0.81 MHz (0.71 km s^{-1}), but were subsequently Hanning smoothed for a final spectral resolution of 1.4 km s^{-1} . The phase center was $18^{\text{h}}00^{\text{m}}30^{\text{s}}.45$, $-24^{\circ}04'01''.5$ (J2000), and the projected baseline lengths ranged from 20 to 230 k λ . Typical system temperatures were 200 to 300 K at transit and the total time on-source was 4 hours. The gain calibrators were NRAO530 (J1733-130) (13° distant) and J1911-210 (17° distant) and the bandpass calibrator was J2232+117. Flux calibration is based on observations of Ceres and a model of its brightness distribution using the Miriad task `smaflux`. Comparison of the derived flux of the quasars with SMA flux monitoring suggests the absolute flux calibration is good to within 15%. The estimated accuracy of the absolute coordinates is $\sim 0.15''$. The uncertainty in the relative positions is better than $\sim 0.01''$.

The data were calibrated in Miriad, then exported to AIPS where the line and continuum emission were separated with the task UVLSF (using only line-free channels to estimate the continuum). Self-calibration was performed on the continuum data, and solutions were transferred to the line data. The continuum and line data were imaged using natural weighting. All channels were cleaned to a flux density limit of $350 \text{ mJy beam}^{-1}$, and individual data cubes were then extracted for each spectral line detected. After combining the calibrated LSB and USB continuum uv-data, the 1σ rms noise level achieved in the continuum image is $6.4 \text{ mJy beam}^{-1}$. The noise level in a single channel of the spectral line images is $110 \text{ mJy beam}^{-1}$. The line data have been corrected for the half channel error in SMA velocity labeling discovered in November 2007. The synthesized beam is $0''.90 \times 0''.79$ at position angle -32° , corresponding to a linear scale of $\sim 1700 \text{ AU}$. The primary beam is $\sim 37''$; these data are insensitive to smooth structures larger than about $10''$.

¹The Submillimeter Array (SMA) is a collaborative project between the Smithsonian Astrophysical Observatory and the Academia Sinica Institute of Astronomy & Astrophysics of Taiwan and is funded by the Smithsonian Institution and the Academia Sinica.

We also recalibrated and imaged the 1.4 mm data from the SMA compact configuration originally published by Sollins et al. (2004) (the details of the observing setup can be found in that paper). Using natural weighting, we achieved a continuum rms of 24 mJy beam⁻¹ and a spectral line rms of 150 mJy beam⁻¹ (per 1.1 km s⁻¹ channel), with a beamsize of 3".1 × 2".6 (P.A.=5.5°). The imaged spectral lines include SiO (5-4), H₂S (2_{2,0} – 2_{1,1}), and HC₃N (25-24).

2.2. James Clerk Maxwell Telescope (JCMT)

We have obtained newly-processed 850 μm SCUBA imaging data of G5.89-0.39 observed at the JCMT² on Mauna Kea, Hawaii. The data were obtained from the Canadian Astronomy Data Center (CADC) repository of SCUBA Legacy Fundamental Object Catalogue.³ The image of the source was constructed from a number of independent observations and has an effective beamsize of 22".9. Further information on the data processing is described by Di Francesco et al. (2008). The total flux density of the source was determined from the image to be 36 Jy. For comparison, the flux density reported in the table of the SCUBA Legacy Catalogue is also 36 Jy (see also Sandell 1994). Due to the nature of the chopped observations, these values should be considered lower limits. In order to be conservative, we have added 36 Jy as the zero spacing flux density to the SMA uv data. With this addition, the total flux density recovered in the high resolution image is 9.6 Jy, or 27%.

2.3. Very Large Array (VLA)

Several archival datasets from the NRAO⁴ Very Large Array (VLA) were calibrated and imaged in AIPS. The observing parameters of these data are summarized in Table 1. Some of the datasets were observed in continuum mode, while others were observed in line mode. In project AZ075, the NH₃ (2,2) and (3,3) transitions were observed simultaneously, each with 6.3 MHz bandwidth (82 km s⁻¹) with 0.195 MHz channel width (2.45 km s⁻¹).

² The James Clerk Maxwell Telescope is operated by the Joint Astronomy Centre on behalf of the Science and Technology Facilities Council of the United Kingdom, the Netherlands Organisation for Scientific Research, and the National Research Council of Canada.

³<http://www4.cadc-ccda.hia-ihp.nrc-cnrc.gc.ca/community/scubalegacy/>

⁴The National Radio Astronomy Observatory is a facility of the National Science Foundation operated under agreement by the Associated Universities, Inc.

2.4. Combined Array for Millimeter Astronomy (CARMA)

Our CARMA⁵ observations were obtained on 12 December 2007 in the B-configuration with 13 antennas (five 10.4m antennas and eight 6m antennas, for a total of 78 baselines). The 225 GHz zenith opacity ranged from ~ 0.19 to 0.23 during the observations. Typical (SSB) system temperatures were 200 to 400 K and the total time on-source was 1.8 hours. The receivers were tuned to an LO frequency of 92.85 GHz. Three continuum bands of ~ 500 MHz width, each comprised of 15 channels, were correlated in each sideband, centered at ~ 89.6 , 90.7 , and 91.2 GHz (LSB) and 94.5 , 95.0 , and 96.1 GHz (USB). Only the bands centered at 90.7 , 91.2 , 94.5 , and 95.0 GHz were used due to the significantly reduced sensitivity on the 6m antennas at IFs above 2.4 GHz. The phase center was $18^{\text{h}}00^{\text{m}}30^{\text{s}}.45$, $-24^{\circ}04'01''.5$ (J2000). The gain calibrator was NRAO530 (J1733-130) (13° distant), the bandpass calibrator was 3C454.3, and the flux calibrator was Uranus. The data were calibrated in Miriad and then self-calibrated in AIPS. The combination of the LSB and USB data imaged with a robust weighting factor of -0.5 yielded a beamsize of $1''.40 \times 0''.90$ at position angle 38° , and an image rms of $1.6 \text{ mJy beam}^{-1}$.

2.5. Infrared images

Several archival images were obtained from the ESO archive, as listed in Table 2. In particular, the data include those published in Feldt et al. (2003) from which those authors identified the proposed exciting source which we call "Feldt's star". The near-infrared ($\lambda < 5 \mu\text{m}$) images were processed with standard techniques: each raw frame was reprojected to a common projection, and the raw frames combined with a median filter to remove outliers and cosmic rays. No sky subtraction was attempted, since we use these images to identify infrared sources and morphology, but not for photometric measurements. Although the relative pointing of raw frames was very accurate, the absolute astrometry of the data were incorrect by up to $10''$. We registered the relatively large field-of-view ISAAC image to 2MASS; since the latter has astrometric uncertainty of less than $0.1''$, this registration is limited by centroiding the ~ 10 stars used, with a resulting uncertainty on the ISAAC frame position of $0.1''$. We then registered the smaller field-of-view NACO frames to the ISAAC

⁵Support for CARMA construction was derived from the states of California, Illinois, and Maryland, the Gordon and Betty Moore Foundation, the Kenneth T. and Eileen L. Norris Foundation, the Associates of the California Institute of Technology, and the National Science Foundation. Ongoing CARMA development and operations are supported by the National Science Foundation under a cooperative agreement, and by the CARMA partner universities.

image using 5–10 stars in each frame, with a total resulting positional uncertainty of $0.2''$. Our positions differ from those of Feldt et al. (2003) by $0.2''$ (our position is nearly directly east of theirs). However, since the offset we find is equal to the uncertainty, for this paper we have chosen to align our near-IR images so that the position of Feldt’s star matches the value published by those authors (18:00:30.44, -24:04:00.9 (J2000)).

The mid-infrared TIMMI2 data required somewhat more detailed processing to remove slowly-changing flat field and detector effects over the course of the observation⁶. We constructed a ”rolling sky” sequence of frames by taking the median of each four frames in chronological order. As the raw frames are chopped and the telescope nodded, each frame consists of a positive sky image minus a shifted negative sky image, with large-scale thermal emission removed. The position of the source changes according to the telescope nod position, so the median of four consecutive frames contains no information from the sky, but information about time-dependent detector variations. The rolling sky is subtracted from each raw frame, those are masked, shifted, and added to form a mosaic image. Finally, that image had to be registered, which was done using the astrometry of the mid-infrared images in Feldt et al. (1999) since we could not find the Brooks image (Table 2) in any publication.

3. Results

3.1. Continuum images

The subarcsecond resolution SMA $875\ \mu\text{m}$ continuum image is shown in Figure 1a. For comparison, we overlay two contours from the lower resolution 1.4 mm image. The north-south extension first noted by Sollins et al. (2004) is now resolved into discrete sources at $875\ \mu\text{m}$; these regions have been labeled for later reference. The submillimeter emission shows a shell-like morphology with an obvious hole in the center. The brightness of the shell varies around its circumference with three major peaks. The easternmost peak lies $0''.25$ east of Feldt’s star. Some emission (SMA-N) extends off the north-northeast side of the shell, and a point source (SMA-S) is seen completely separate from the shell to the south-southwest. The point of lowest brightness in the UCHII shell is on the southeast side and may indicate an opening in the shell. Further to the south-southeast, we find faint filamentary emission that appears to trace a coherent structure. No $875\ \mu\text{m}$ continuum emission was found outside the field shown in Figure 1a.

⁶See the TIMMI2 documentation http://www.ls.eso.org/lasilla/sciops/3p6/timmi/html/t2_overview.html for more information.

Our 2 cm image is shown in Fig 1b. This is the highest resolution and sensitivity image to date of G5.89-0.39 at radio wavelengths shorter than 3.6 cm. As seen in the original 2 cm survey image of Wood & Churchwell (1989), the dominant feature is a shell-like structure surrounding a central cavity of diameter $\approx 1''$. The elongated low-level emission surrounding the shell evident along a position angle of $\approx -28^\circ$ has been known since the original 6 cm VLA A-configuration image of Zijlstra & Pottasch (1988). In our new image, we find a nearly-closed loop of emission extending along this direction on the northwest side of the shell (also see Acord et al. 1998). Like the 875 μm image, the 2 cm image shows a break in the SE edge of the shell, suggesting a "blow-out" of ionized gas in this direction. We note that the southern portion of the elongated ionized emission is not exactly coincident with the extension seen at 875 μm , but instead lies to its SW.

For comparison, the SMA 875 μm and VLA 2 cm images are shown alongside a wide range of other centimeter to near-infrared wavelength images in Figure 2. All of the radio through submillimeter images have been generated from data with a comparable range of uv spacings, have been restored with the same beam ($1''.40 \times 0''.90$ at P.A.= $+35^\circ$), and are displayed with the same flux density color scale. The beam was chosen to match the beam of the poorest resolution dataset (3 mm). At the lowest frequency (6 cm), the central part of the UCHII region shows a roughly uniform appearance. As one moves to higher frequency, the source brightens, and the shell structure emerges and becomes increasingly distinct. This change in appearance is due to the decreasing optical depth of free-free emission as the observed frequency increases.

To further demonstrate the effect of free-free optical depth, we measured the flux density in a single beam at various positions in the UCHII region (using the images in Figure 2) as well as the total emission in the field within an $12''$ box (see Table 3). The corresponding spectral energy distributions (SEDs) are plotted in Figure 3. At centimeter to millimeter wavelengths, the data are consistent with free-free emission with a turnover at about 2 cm. The excess emission at 875 μm toward SMA1 and SMA2 suggests the presence of dust toward these positions. In order to quantify this component, we must estimate and remove the free-free contribution to the 875 μm emission. The common analytic approximations for free-free emission given by Altenhoff et al. (1960) and Scheuer (1960) become less accurate above 100 GHz. Thus, we have used the numerical calculation of the Gaunt factor for free-free radiation along with Equations 2 and 15 given by Beckert et al. (2000). Using the non-linear fitting utility of Matlab (lsqcurvefit), we produced the SED fits shown in Figure 3. The resulting electron temperatures and emission measures range from 9000 K and $3.0 \times 10^8 \text{ cm}^{-6} \text{ pc}$ at the central position to 12000 K and $8.3 \times 10^8 \text{ cm}^{-6} \text{ pc}$ close to Feldt's star. For the integrated emission, the corresponding values are 8500 K and $3.5 \times 10^8 \text{ cm}^{-6} \text{ pc}$. Assuming the source has equal extent in the third dimension as it does in the plane of the

sky ($4''$ or 0.039 pc) this average emission measure corresponds to an average electron density of $\sim 10^5 \text{ cm}^{-3}$. However, this estimate does not take into account the shell-like structure of the UCHII, and in fact the width of the shell is only marginally resolved with $0''.7$ resolution, implying that significantly higher n_e are present in the shell.

Based on these results, we followed two methods for deriving a free-free emission map at $875 \mu\text{m}$ and compared their results. The first and simplest method consisted of choosing a characteristic temperature (10000 K) and emission measure ($4 \times 10^8 \text{ cm}^{-6} \text{ pc}$), computing the expected flux density scale factor between 1.3 cm and $875 \mu\text{m}$, and applying it uniformly to all pixels in the 1.3 cm image. The scale factor (0.715) corresponds to an effective spectral index of -0.154 from 1.3 cm to $875 \mu\text{m}$ ⁷. This spectral index is in good agreement with the values used in recent attempts to quantify the Galactic foreground contribution to CMB studies (see for example Dickinson et al. 2003). The extrapolated free-free image was then subtracted from the observed $875 \mu\text{m}$ image in order to generate an image of dust emission, shown in Figure 4. Due to the subtraction, the image rms is increased by $\approx \sqrt{2}$ to 10 mJy beam^{-1} , thus it has been masked at the 5σ level (50 mJy beam^{-1}).

For the second method, we first computed the ratio of the 1.3 cm and 3 mm images, then solved for the emission measure as a function of pixel that would theoretically produce the observed ratio, assuming isothermal 10000 K gas. The result is an emission measure image (shown in Figure 4), which we then used to generate a synthetic free-free image at $875 \mu\text{m}$, which we finally removed from the observed $875 \mu\text{m}$ image. The resulting dust image closely matched that generated by the simpler method, as seen in the “model difference” image in Figure 4. The largest differences are less than 5σ when compared with the rms in the observed $875 \mu\text{m}$ image.

Five discrete areas of dust emission are evident, and their positions and flux densities are tabulated in Table 4. SMA1 and SMA2 are compact sources which lie on or near the UCHII shell, SMA-S is compact and lies outside of the shell, and SMA-N and SMA-E are more extended and also lie outside of the shell. As can be seen in the VLA images (Figure 2), there is no corresponding centimeter wavelength emission toward the positions denoted SMA-N, SMA-S, and SMA-E; thus we conclude that this emission is from dust. We note that the locations of SMA-N and SMA-S lie along an axis defined by the southern cluster of OH masers (Stark et al. 2007) and passing through the center of the UCHII shell. Further south, the filamentary structure of $875 \mu\text{m}$ emission must also arise from dust as there is no evidence for it in the centimeter images, which have more than adequate sensitivity to have

⁷While it should be noted that the scale factor determined in this manner is slightly dependent on the electron temperature, it changes by $< 0.1\%$ for temperatures in the range of $7500\text{-}15000 \text{ K}$.

detected it (if it was free-free emission). We note that there is no evidence for dust emission near the center of the UCHII shell. The $875\ \mu\text{m}$ flux density from dust at the position of Feldt’s star is $10\ \text{mJy beam}^{-1}$ which is equal to the 1σ noise level. For comparison, if we use our astrometry for Feldt’s star, the flux density from dust would be $31\ \text{mJy beam}^{-1}$.

3.2. Infrared images

Images at $1.7\ \mu\text{m}$, $2.12\ \mu\text{m}$ (K_s band) and $11.9\ \mu\text{m}$ (N band) are shown in the bottom row of Figure 2; Feldt’s star is indicated by the open star symbol. The cometary shape of the mid-infrared emission toward G5.89-0.39, coinciding with the northern half of the UCHII shell, has been noted previously (Ball et al. 1992). However, the N band image also shows evidence for two distinct peaks within the cometary emission. The position of the brighter N band peak is coincident with that of SMA1 (i.e. within the combined astrometric uncertainties). Similarly, the fainter peak coincides with Feldt’s star. In agreement with Puga et al. (2006), we find that most of the K_s band emission in the field shown in Figure 2 is continuum rather than H_2 , with the exception of the sources A, D1, and D2 denoted by Puga et al. (2006). We also examined *Spitzer* IRAC data for this region but with its poorer angular resolution ($> 2''$) the mid-IR emission appears as a featureless blob. Comparison of the narrow band $1.2\ \mu\text{m}$ image (not shown, see Table 2) with the $1.7\ \mu\text{m}$ image shows that all four of the bright stars in the upper half of the $1.7\ \mu\text{m}$ image shown in Figure 2 are also detected at $1.2\ \mu\text{m}$, with the star nearest SMA1 being the faintest. It is likely that all four stars are foreground to the nebula.

3.3. Spectral line images

Over three dozen spectral lines were detected in our SMA observations (see Table 5). Eighteen of them were detected with a high signal-to-noise ratio and suffer minimal confusion from line blending. To inspect the spatial distribution of emission in these lines, we created total intensity moment zero images using the total observed velocity extent of the emission, determined for each line independently. Contour maps of these images are shown in Figures 5 and 6 superposed on the $875\ \mu\text{m}$ continuum image. In Figure 6, the images of two vibrational lines of SO_2 have been averaged before displaying the contour map. In addition, we detect three faint vibrationally-excited lines of HC_3N which we have similarly averaged in order to create the contour map in Figure 5.

Figure 5 shows contour maps of a mixture of species, including high-density tracers,

high column-density tracers and outflow tracers. As with the dust, none of these gas species show emission inside the UCHII shell, suggesting a cavity at this location. Only CO, C¹⁷O, CH₃OH, C³⁴S, and H¹³CO⁺ exhibit emission significantly (4'') outside of the UCHII ring. Particularly in the southern part of the images, these molecules appear to be tracing the filamentary structures seen in dust emission (§ 3.1). In some cases (CH₃OH and C³⁴S), the molecules follow the inner edge of this structure rather than the structure itself. Faint emission from H¹³CO⁺ and C¹⁷O is also found along this structure. In contrast, the near-IR H₂ features A, D1, and D2 (Puga et al. 2006) appear along the outer boundary of this structure. The strongest emission from HC₃N, C¹⁷O, and H¹³CO⁺ traces a ridge along the northern and western edges of the UCHII. The latter molecule peaks a fraction of an arcsecond further outward and is the best tracer of the boundary of the mid-infrared emission. In addition, these three molecules show an extension toward the north-northeast which appears to be associated with the dust source SMA-N. Other molecules also appear in this vicinity, including CH₃OH (also seen at this location by Sollins et al. (2004)), SiO, and C³⁴S. This emission is fairly broad ($\Delta v \sim 12 \text{ km s}^{-1}$). An additional point source of gas emission very close to the location of the dust source SMA-E is seen in H¹³CO⁺, HC₃N, CH₃OH, and C¹⁷O. Compact peaks of C¹⁷O and HC₃N are also seen at the position of SMA2.

Figure 6 shows integrated intensity contour maps of emission in nine lines of SO, SO₂ and their isotopologues in our SMA bandpass. On the east and west sides of the UCHII ring, the peak emission from the most abundant species appears to trace ridges that form a border *outside* of the free-free emission. The position angles of these ridges are -24° and -26° on the east and west sides, respectively. In contrast, on the north side, the line peaks *coincide* with the ridge of free-free emission. Toward the southeast side, there is no line emission, further suggesting an incomplete shell in this direction. The less abundant isotopologues show peaks at the positions of SMA1 and SMA2, as do the vibrationally-excited lines of SO₂ and HC₃N (Fig. 5), indicating high column densities of warm gas. The vibrationally-excited lines also show an isolated peak $\sim 1''$ east-northeast of Feldt’s star. The spectra toward SMA-N are significantly broader than toward SMA1 or SMA2 and the line wings in HC₃N and C³⁴S extend to redder velocities (see Figure 7). This is the same velocity shift detected in lower angular resolution data, including the OVRO observations of CH₃CN (Akeson & Carlstrom 1996) and the SMA observations of SiO (5-4) (Sollins et al. 2004).

The molecular gas shows complicated velocity structure in many of the species. Figure 8 shows first moment maps of several species. Perhaps best seen in SO₂, the primary feature is a change from redshifted emission on the northeast side of the UCHII to the LSR velocity ($\sim 9 \text{ km s}^{-1}$) emission on the northwest and southwest sides. The magnitude of the shift is approximately 4 km s^{-1} . The gas located in the filamentary dust structure near the southern edge of the images lies at the LSR velocity. A blueshifted component is seen in

SO₂ at the southern edge of the UCHII. The CH₃OH and C³⁴S show redshifted emission toward SMA-N (see Fig 7). Redshifted emission is also seen in SiO (8-7) near SMA-N, while blueshifted emission is seen in the vicinity of SMA-S. At lower angular resolution these two spatial components were interpreted as a bipolar outflow by Sollins et al. (2004). Although these areas of SiO emission lie along an axis including Feldt’s star, the emission does not extend back to it. Having seen these results, we reanalyzed the lower frequency SMA data from Sollins et al. (2004) and present channel maps of three lines in Figure 9. Clearly, the SiO (5-4) emission is more complicated than a single spatial velocity gradient at position angle +28°. In fact, the emission in all three of these lines demonstrate the complexity of the molecular emission within $\pm 15 \text{ km s}^{-1}$ of the systemic velocity. One is thus driven to studying higher velocity gas in order to seek the origin of bipolar outflow emission in this region.

The high abundance of the CO molecule provides the best chance to study the high velocity molecular gas. Contour maps showing the kinematics of CO (3-2) are shown in Figure 10. In the midst of the complexity of this emission, we identify a linear bipolar structure at high velocities at position angle -4°. The axis defined by this structure passes through the dust core SMA1 and intercepts highly redshifted CO emission north of the UCHII along with a Class I methanol maser (component 2 of Kurtz et al. (2004)). Two redshifted clumps of CO emission correspond in position to the redshifted knots C1 and C2 of the near-IR H₂ emission (Puga et al. 2006). A highly redshifted (+78 km s⁻¹) water maser feature (Hofner & Churchwell 1996) also lies along this axis near the far northern extent of the CO emission. Toward the south, the blueshifted knots of the near-IR H₂ emission (component A) lie near the peak of the blueshifted CO. Water masers are also found along the southern portion of the bipolar axis, including a moderately blue-shifted component at -3.2 km s⁻¹ at the southernmost maser spot. A higher velocity blueshifted component was once seen at -61 km s⁻¹ in single-dish observations by Genzel & Downes (1977) but has not been detected in subsequent VLA observations, possibly due to variability. Most of the known OH masers, specifically the collections of spots denoted G5.89 Center and G5.89 South (Stark et al. 2007), are clustered in close proximity to the southern axis of this north-south bipolar structure and predominantly exhibit the appropriate highly blueshifted velocities ($\sim 30\text{-}40 \text{ km s}^{-1}$ from the LSR). A notable exception is the southernmost group of masers in G5.89 South which occur the southern edge of the UCHII region and have a small redshifted velocity (from 11-15 km s⁻¹). At the same position and velocity, we see compact emission in the lowest energy SO₂ line, which appears as a peculiar red feature in the first moment map (Figure 8). The other collection of OH masers, G5.89 East, lies furthest from the bipolar axis and most of its members have velocities near the LSR, suggesting that it is unrelated to the north/south structure.

To further explore the north/south bipolar structure, we reimaged and analyzed the data from the Berkeley-Illinois-Maryland Array (BIMA) published by Watson et al. (2007). Of the four molecular transitions observed, the HCO^+ (1-0) line had the widest velocity coverage (131 km s^{-1}). With a resolution of $8''.5 \times 3''.5$, we find the same north-south velocity gradient in HCO^+ emission as is seen in our CO (3-2) data and the maser data. Contour maps of the red and blueshifted BIMA HCO^+ emission are also shown in Fig 10. The sense and direction of the velocity gradient in CO (3-2) and HCO^+ match that seen in a C^{34}S (3-2) map obtained with a $17''$ beam at the IRAM 30m telescope (Cesaroni et al. 1991). Finally, in Figure 10 we have also plotted the highest velocity emission from the SMA SiO (5-4) data, extending beyond the range shown in the channel maps in Figure 9. Again, the velocity gradient follows a position angle close to the other lines.

3.4. NH_3 (3,3) maser emission

The NH_3 (3,3) transition shows a complex arrangement of weak emission outside the UCHII region and absorption toward the shell, consistent with the lower resolution data presented by Gomez et al. (1991) and Wood (1993). However, we have discovered an intense point source of emission located at $18:00:29.539, -24:03:52.65$ (J2000), which is $\approx 12''$ northwest of the UCHII region (see Fig 11). The fitted line peak is at $\sim 11.2 \text{ km s}^{-1}$, but the emission is not spectrally resolved with the 2.45 km s^{-1} velocity resolution of these data (the emission is spread over two channels). After correction for primary beam attenuation and using uniform weighting to construct the image, the peak flux density is $31.3 \pm 3.0 \text{ mJy beam}^{-1}$, corresponding to a lower limit for the peak brightness temperature of $808 \pm 80 \text{ K}$ at a resolution of $0''.52 \times 0''.23$. This temperature is significantly higher than expected for thermal excitation and indicates weak population inversion. Other examples of objects where this NH_3 transition is found to be inverted include the high-mass star-forming regions DR21(OH) (Mangum & Wootten 1994), NGC 6334 (Kraemer & Jackson 1995; Beuther et al. 2007), W51 (Zhang & Ho 1995), and IRAS 20126+4104 (Zhang et al. 1999). In all cases, these masers are located in or at the ends of high velocity protostellar outflows. In G5.89-0.39, the peak position and velocity of the NH_3 maser are coincident (to within $0''.27$ and 1.0 km s^{-1}) with a Class I CH_3OH maser observed with the VLA (component 1 of Kurtz et al. (2004)), which is another outflow tracer. G5.89-0.39 is only the second object in which these two maser transitions have been found to coincide spatially, the other example being DR21(OH) (Mangum & Wootten 1994). Interestingly, the NH_3 maser is also located within $3''$ (north-northeast) of the near-IR knot B of Puga et al. (2006). As shown in Figure 11, these objects lie close to the axis (position angle = -54°) of the $\text{Br}\gamma$ outflow identified by Puga et al. (2006) as do the near-IR knots D1 and D2. Figure 11 summarizes

these new results within the context of the CO (1-0) outflow map from Watson et al. (2007).

4. Discussion

In order to interpret our unprecedented subarcsecond submillimeter images, we have assembled a comprehensive dataset on this object. The multiwavelength nature of our work warrants a fresh examination of the morphology of the UCHII region, the nature of the ionizing source, the number and structure of the outflow(s), and the presence of young stellar objects in this important region.

4.1. Shape and structure of the ionized nebula

UCHII regions are divided into a number of morphological classes (Wood & Churchwell 1989), with one of the rarer classes being “shell-type”. G5.89-0.39 is perhaps the most distinctive and well known member of this class with a well-defined central cavity with a radius approximately one-third that of the outer UCHII radius. Our new subarcsecond submillimeter observations have revealed that this cavity is devoid of dust, as would be expected when a strong ionizing source is present within the shell (Churchwell et al. 1990; Faison et al. 1998). A striking result from our molecular line images is that, at subarcsecond scales, no species are seen on the line of sight to Feldt’s star, indicating a low column density of obscuring material close to the star. This result is a vivid demonstration of why this star can be seen at near-IR wavelengths. In the discovery paper, it was noted that Feldt’s star is significantly offset from the center of the cavity, and the possibility of proper motion as an explanation was discussed. At present, there is no knowledge of the velocity of the star with respect to the UCHII region or the molecular gas. Another explanation that may apply to G5.89-0.39 comes from recent modeling of the dynamical expansion of UCHII regions in self-gravitating molecular clouds, which demonstrate that nearly spherical shells can be produced even if the ionizing star is off center (Mac Low et al. 2007). In any case, our data provide no counter evidence to the hypothesis that Feldt’s star is the ionizing source of the UCHII region.

Now we turn our attention to the cm emission just outside of the shell. Ever since the original VLA A-configuration 6 cm image (Zijlstra & Pottasch 1988), the elongation of the low-level cm halo of G5.89-0.39 has been evident along a position angle of $\approx -28^\circ$. In our SMA spectral line images, we now see that the distribution of the molecular gas traced by SO₂ follows this same position angle as it effectively encompasses and bounds the UCHII

region on two sides (see the upper left panel of Fig. 6). The morphology of this line emission suggests that the molecular gas is being driven outward by the expansion of the UCHII region. The velocity shifts seen in the first moment maps (Fig 8) suggest that 2 km s^{-1} is a lower limit to the expansion rate (because an additional component of motion could be present transverse to the line of sight). The fact that the molecular gas on the northwestern side of the UCHII peaks on the shell rather than outside of it, in contrast to the northeast and southwest sides, suggests that molecular gas is missing from the northwestern “cap”. This arrangement would explain the position angle of the northern elongation of the cm halo. The possibility that the ionization front is also “blowing out” in the southeastern direction was previously suggested by Ball et al. (1992). Our observations support this suggestion in two respects: we see a break in the $875 \mu\text{m}$ continuum emission at the point where this southeastern axis intersects the UCHII shell, and we see extended source of dust emission (SMA-E) located radially outward from this break. The fact that nearly all of the dust emission lies within a few arcseconds of the outer edge of the UCHII region is a result that agrees with predictions from previous infrared observations (Harvey et al. 1994).

4.2. Location of Molecules

As seen in single dish spectra (Thompson & MacDonald 1999), we find G5.89-0.39 to be almost completely lacking in organic molecular line emission while being rich in sulfur-bearing molecules. This result is in sharp contrast to observations of massive young stellar objects (with hot cores) with the same spectral setup and angular resolution with the SMA (see e.g. Brogan et al. 2007a). Based on JCMT line profiles of G5.89-0.39, Thompson & MacDonald (1999) suggest that HC_3N traces the envelope surrounding the UCHII while the sulfur and silicon-bearing species with broad lines trace an outflow. Our images confirm that HC_3N emission is located primarily along the northwestern half of the UCHII shell, and that much of the SiO and C^{34}S is found at larger distances from the UCHII. However, as described in sections 3.3 and 4.1, we find that SO and SO_2 are also concentrated primarily around the shell, apparently constraining the expansion of the UCHII region. They do not show any obvious evidence of tracing the beginnings of the larger scale east/west outflow reported in CO (Klaassen et al. 2006; Watson et al. 2007). Instead, the optically-thin isotopologues of SO and SO_2 appear to be tracing compact regions of emission at the LSR velocity, similar to C^{17}O and HC_3N . At least two of these compact regions of line emission are coincident with the dust cores SMA1 and SMA2, while a third may be associated with the $\text{Br}\gamma$ outflow source described by Puga et al. (2006) (see Figures 5 and 6).

East of SMA-S, there is an arc-like structure seen in CO , CH_3OH , and C^{34}S just north

of a similar filamentary structure seen in dust emission. Moreover, emission from the high column density tracers C^{17}O and H^{13}CO^+ coincides with the dust emission. It is unclear whether this morphology is associated with the expansion of the UCHII region or is an independent structure. Remarkably, SMA-S itself is nearly free of line emission in our data. We find this to be an enigmatic source, similar to NGC6334I SMA4 (Hunter et al. 2006). It could be a very young protostellar object in which most common gaseous species are frozen onto grains. Following the method described in § 4.3, we estimate the total mass of SMA-S to be 12-20 M_{\odot} assuming the temperature is in the range of 15-20 K. This amount of mass is sufficient to be an intermediate mass pre-protostellar core. Future high-angular resolution observations in other species that remain in the cold gas phase longer in the evolutionary sequence, such as N_2H^+ and H_2D^+ (Flower et al. 2006), would be useful in studying this object.

4.3. The Nature of SMA1 and SMA2

There are a growing number of examples of chemical complexity on arcsecond scales in regions of massive star formation. One reason for this complexity is the superposition of multiple young stellar objects at slightly different LSR velocities, as in, for example Cep-A East, (Brogan et al. 2007b; Comito et al. 2007). The SMA images of G5.89-0.39 have a spatial resolution of < 2000 AU, which is finer than the typical separation of members of protoclusters (Hunter et al. 2006). Thus we are able to resolve the emission from individual objects and compare their line strengths in various chemical species. The set of spectral line profiles in Figure 7 shows that the ratio of the strength of HC_3N to SO and SO_2 is larger in SMA1 than in SMA2, as is the ratio of C^{17}O to SO and SO_2 . The high critical density and excitation temperature of the submillimeter HC_3N transitions makes them an excellent tracer of warm dense gas, as is seen in many high-mass star forming regions observed at high angular resolution (Cyganowski et al. 2007; Mookerjee et al. 2007; Wright et al. 1996). Also, the strong detection of the C^{17}O (3-2) line requires a large column density of moderately warm gas. The relatively greater strength of these two lines in SMA1 combined with its detection at $11.9\mu\text{m}$, and association with the north/south bipolar outflow suggests that SMA1 likely contains a protostar. SMA2, being richer in sulfur-bearing molecules, likely has a greater fraction of its molecular excitation due to shocks, and it is less clear that it harbors a protostar. We have fit the line profiles toward SMA1 and SMA2 with single Gaussians (Table 6) and find that SMA2 is somewhat broader (by 1 km s^{-1}) and bluer (by 0.5 km s^{-1}), supporting our conclusions.

Unfortunately, it is difficult to estimate the luminosities of SMA1 and SMA2 due to

the lack of arcsecond resolution images between $20\mu\text{m}$ (Feldt et al. 1999) and $875\mu\text{m}$. The $11.9\mu\text{m}$ detection of SMA1 cannot accurately constrain the peak of the dust spectral energy distribution or the dust temperature. The best hope for further progress in the near future would be to measure the gas temperature. One can imagine constructing a rotation diagram from our dataset using the multiple transitions from SO_2 . However, this molecule is clearly very optically thick, as its isotopologues rival the main line in brightness, and they have somewhat smaller linewidths. Thus, an optical depth correction is essential, but this can only be done using a pair of transitions from the same energy level. Although we do have one such pair (SO_2 $19_{1,19} - 18_{0,18}$ and $^{33}\text{SO}_2$ $19_{1,19} - 18_{0,18}$), the comparison is complicated by the hyperfine structure of $^{33}\text{SO}_2$. Accurate temperature measurements of SMA1 and SMA2 will require a more extensive combination of spectral lines and isotopologues than are found in the present SMA data. In the meantime, a lower limit to the temperature can be obtained from the brightness temperature of the brightest line (in both cases it is an SO_2 line). For SMA1, this value is 34 K, and for SMA2 it is 65 K. When compared to the brightness temperatures of the dust emission in Table 4, these values yield upper limits to the $875\mu\text{m}$ dust optical depth of 0.066 and 0.10. Using these values along with the dust continuum flux densities, one can derive an upper limit estimate for the mass. In the case of SMA1 and SMA2, we use the peak flux densities in order to assess the unresolved point source component at these positions. Following Equation 1 of Brogan et al. (2007b), in which $\kappa_{875\mu\text{m}} = 1.84\text{ cm}^2\text{ g}^{-1}$ and the gas to dust mass ratio is 100, we find upper limits of 6 M_\odot and 2 M_\odot for SMA1 and SMA2, respectively. For comparison, if the dust temperature is 100 K, the corresponding masses would be 1.6 M_\odot and 1.3 M_\odot .

Our observations of C^{17}O (3-2) provide an independent estimate of the mass of SMA1 and SMA2. C^{17}O has a well-known abundance with respect to H_2 of 4.7×10^{-8} (Frerking et al. 1982) and has been used in single dish studies of other ultracompact HII regions (Hofner et al. 2000). At the moderately warm temperatures of SMA1 and SMA2, the possible confounding effect of depletion of C^{17}O onto grains should be minimal, as the desorption temperature is likely in the range of 15-40 K (Jørgensen et al. 2006; Doty et al. 2004). We have measured the integrated intensity of C^{17}O towards these objects, and used the equations of Mangum & Shirley (2006) to determine the column density in the optically-thin, Rayleigh-Jean limit. Using the peak brightness temperatures of the line, we estimate the optical depths to be small as long as the excitation temperature is above $\sim 30\text{ K}$. In Table 7, we list the opacity, column density and mass ($0.9\text{--}1.6\text{ M}_\odot$) computed for excitation temperatures of 75 K and 150 K. The column density and mass have been corrected for opacity. The values at 75 K are only about 20% higher than the minimum values one would obtain if the excitation temperature was set equal to the upper state energy (32.3 K). A temperature of 100 K provides good agreement between the dust-derived and C^{17}O circumstellar mass, and also

provides a greybody model consistent with the submillimeter and mid-IR flux densities at the position of SMA1. Indeed, based on mid-infrared images at 11.7 and 20 μm , Feldt et al. (1999) derive a temperature of 120 K for the hot dust component at the position of SMA1. Using a temperature of 100 K, the total luminosity of SMA1 is $\sim 3000 L_{\odot}$. For reference, on the main sequence this luminosity corresponds to an early B star with a central stellar mass of 7.5 to 8.5 M_{\odot} depending on the mass-luminosity relation used (Demircan & Kahraman 1991; Hilditch & Bell 1987).

In any event, the circumstellar masses we obtain for SMA1 and SMA2 are comparable to the upper limits measured for the BN and IRc2 objects in Orion (Eisner & Carpenter 2006), and to circumstellar masses surrounding intermediate mass protostars (Beltran et al. 2007; Neri et al. 2007). However, we emphasize that the nature of SMA2, including whether or not it contains a central heating source, remains unclear, particularly because it lacks a clear association with a bipolar outflow (unlike SMA1). The locations of SMA1 and SMA2 with respect to the UCHII region shell and their gas masses are broadly consistent with simulations of “secondary collapse” by Mac Low et al. (2007). In the Mac Low et al. (2007) model, gravitational instabilities in the material swept up in an expanding UCHII region shell can produce a second generation of collapsing cores in the shell with masses of a few M_{\odot} . Quantitative predictions for the dust emission from such cores are not made, but the prediction for the free-free emission that would be present at the boundary between the ionized gas and dense core of a few 100 mJy is consistent with the observed free-free emission in the vicinity of SMA1 and SMA2.

The lack of organic “hot core” emission from SMA1 (and SMA2 if it also contains a protostar) has several possible explanations: (1) the protostar may be of sufficiently late type (low mass) to preclude the formation of a hot core. However, as already discussed the circumstellar mass is consistent with those of intermediate mass protostars, and such sources are capable of producing hot core line emission (see for example Fuente 2008). (2) The protostar could be sufficiently young that it has not yet reached the hot core phase, but this seems less likely given the presence of the energetic north/south outflow from SMA1. (3) The progenitor of the UCHII region (presumably Feldt’s star) may have melted enough of the icy dust mantles in its vicinity during its formation that the reservoir of organic material was severely depleted for later generations of protostars. (4) Although the simulations of Mac Low et al. (2007) show that the column densities of the “secondary collapse” cores are not disrupted by the passage of the UCHII shock, the effect on the chemistry of such cores has not been assessed. Thus it is possible that the passage of the UCHII shock destroyed the fragile organic molecules. Higher angular resolution study of the dust emissivity and molecular line emission with ALMA in the future will help distinguish between these possibilities.

4.4. Origin of the outflows

What do our SMA data reveal about the massive outflow from G5.89-0.39? First of all, the 875 μm line emission shows some evidence of a general expansion centered on the UCHII region. The location of the clump of molecular line emission associated with SMA-N combined with the ridge of dust, C^{17}O , and H^{13}CO^+ emission in the south suggest that Feldt’s star is more likely than SMA1 to be the origin of this activity. Regarding the large-scale east/west CO outflow, there is no obvious bipolar structure tracing back to Feldt’s star or any of the dust cores along the position angles quoted by Klaassen et al. (2006) and Watson et al. (2007). This result is consistent with the “extinct jet” hypothesis of Klaassen et al. (2006), whereby the large scale outflow is a remnant flow from a previous generation of protostellar activity. However, our CO(3-2) and $\text{HCO}^+(1-0)$ images do show direct evidence for a collimated bipolar outflow originating from SMA1 at position angle -4° , lending further weight to our identification of it as a protostar. This outflow matches the outflow direction postulated by Puga et al. (2006), as it naturally explains the arrangement of the near-IR H_2 knots A and C. In addition, this outflow explains the geometry of most of the maser emission spots in this region, including H_2O , OH, and Class I CH_3OH masers. In particular, the locations and kinematics of the high-velocity H_2O maser components to the north and south of the UCHII region, along with the blueshifted OH masers to the south, follow the CO and HCO^+ velocity field centered on SMA1 (see Fig. 10).

In addition to the outflow from SMA1, we also find tentative evidence for a second outflow in redshifted and blueshifted CO emission and blueshifted HCO^+ emission, centered on the Br γ outflow origin, with a position angle of -54° , similar to that found by Puga et al. (2006). The near-IR knots to the northwest and southeast (B and D) are aligned roughly with this axis, as is the new NH_3 (3,3) maser. It seems likely that all of these phenomena are outflow-related, and have a common driving source. We find a point source of emission from vibrationally-excited SO_2 and HC_3N at this position (see Fig. 5 and 6), suggesting a central powering source at this location. While we do not find a compact dust source at the origin, it does lie at the ~ 200 mJy level within a ridge of dust emission associated with the northwest edge of the UCHII region. We estimate an upper limit of ~ 80 mJy for a point source at this position, which corresponds to a mass upper limit of $\sim 0.4 M_\odot$ (assuming a temperature of 65 K), comparable to gas masses found to be surrounding intermediate-mass protostars (Beltran et al. 2007; Neri et al. 2007). Another explanation for knots B and D and the (3,3) maser is that they are simply enhancements in the large-scale east/west outflow. The fact that the NH_3 maser (and its associated CH_3OH maser) sit at the edge of the large blueshifted CO (1-0) outflow lobe (Figure 11) and emit near the LSR velocity is consistent with them originating from a velocity coherent column of shocked gas moving transverse to the line of sight, which is an ideal geometry for generating strong maser features (see e.g.

Liljeström & Gwinn 2000).

One question that arises from the work presented here is the relative ages of the compact north/south outflow from the protostar SMA1, the large scale east/west outflow, the UCHII region and Feldt’s star. We can estimate the timescale for the north/south outflow from SMA1. Using the velocity (w.r.t. the G5.89 LSR of 9 km s^{-1}) and projected offset of the northern H_2O maser relative to SMA1, (69 km s^{-1} and 0.073 pc , respectively), the outflow timescale is $1030 (69/v_{rad}(\text{km s}^{-1}))(1/\tan(i)) \text{ yr}$ (v_{rad} is the radial velocity of the outflow and i is the angle between the line-of-sight and the outflow direction). Using the southern CO (3-2) emission, the timescale is about 1700 years, yielding an average timescale of $\sim 1400 \text{ yr}$. For comparison, the timescale for the motion of H_2 knot A is 400 yr (Puga et al. 2006). Although the timescale for the north/south CO outflow is only a lower limit on the outflow age, it is a factor of five discrepant from the 7700 yr age reported by Watson et al. (2007) based on BIMA CO (1-0) data. However, the velocity ranges used by Watson et al. (2007) in computing the age do not include the high velocity gas that is present in the north/south outflow and are more appropriate to the lower velocity east/west outflow. The timescale we derive for the north/south outflow is closer to the value of 2000 yr reported by Klaassen et al. (2006). This agreement makes sense, because the highest-velocity CO (3-2) emission is unresolved in their single-dish maps, since those spectral channels are completely dominated by the compact outflow from SMA1 rather than the larger, older east/west outflow.

The question remains as to the driving source of the east/west flow. The width of the east/west outflow combined with the confused velocity field within 15 km s^{-1} of the LSR prevents any constraint on the outflow origin to better than a few arcseconds. As an additional source of uncertainty, if the driving source has a small relative motion of 1 km s^{-1} , it could have moved $\sim 0''.8$ during 7700 yr . Two possible candidates are Feldt’s star and SMA2. Lacking direct evidence for an internal heating source in SMA2, we find the most natural scenario for the east/west outflow is that it was driven by Feldt’s star prior to the creation of the UCHII region. The expansion of the UCHII region has disrupted the velocity field around it making it impossible to trace this outflow back to its origin. For the same reason, there could be additional bipolar outflows present (e.g. from other embedded YSOs) that are difficult to discern in this complex velocity field.

Finally, a possible clue regarding the relative age of the outflow from SMA1 and the UCHII region may be found in the fact that the southern lobe of the outflow only appears distinctly in the CO (3-2) contour maps in the regions outside the boundary of the UCHII region. One could argue that the outflow from SMA1 predates the UCHII region, which has recently expanded and disrupted the inner portions of the bipolar morphology, leading to the OH masers. Alternatively, if the UCHII region is significantly older than the proposed 600 yr

age (Acord et al. 1998) and SMA1 is located behind it, then the southern lobe of the outflow from SMA1 may have recently drilled through the UCHII region, creating the OH masers on the front side, and continuing on south of the UCHII region. In this picture, the absence of high velocity redshifted OH features north of SMA1 would be explained by the high optical depth of the UCHII region at 1.6 GHz. We believe the former picture seems more physically plausible, given the lack of a disturbance in the ionized gas morphology along the outflow direction (i.e. the position angle of the low-level centimeter emission differs from the outflow by 24°). In either case, our observations provide further evidence that the OH masers in G5.89-0.39 are associated with a protostellar outflow, a conclusion originally reached by Zijlstra et al. (1990). Other examples of this correlation have been found, for example the TW object of W3(OH) (Argon et al. 2003). Proper motion measurements of the OH masers in G5.89-0.39 should provide valuable insight on this phenomenon.

5. Conclusions

Our subarcsecond submillimeter images of the ultracompact radio source G5.89-0.39 (W28 A2) have shed new light on this enigmatic source. By using a comprehensive set of lower-frequency images, we have modeled and removed the free-free emission and find five residual sources of dust emission. With no dust emission located inside the shell, our observations support the previously-proposed picture of a dust-free cavity located inside a shell-like UCHII region with warm, high-density gas and dust tracing its periphery. Two of the compact dust objects, SMA1 and SMA2, exhibit compact spatial peaks in one or more of the optically thin tracers ^{33}SO , $^{34}\text{SO}_2$, and C^{17}O . In CO (3-2) emission, we have identified a well-collimated, high-velocity outflow from SMA1 at position angle -4° and conclude that it is an embedded intermediate-mass protostar, surrounded by $\approx 1 M_\odot$ of circumstellar material at a temperature of approximately 100 K, and corresponding to the brightest source in the $11.9 \mu\text{m}$ image. The outflow from SMA1 explains much of the near-IR H_2 and centimeter wavelength maser emission in the region. We also find tentative evidence for a second CO outflow associated with the $\text{Br}\gamma$ outflow identified by Puga et al. (2006). The position angle of this outflow points toward the location of a new NH_3 (3,3) maser that we have discovered $12''$ northwest of the UCHII region. The origin of this outflow is marked by compact emission in vibrationally-excited transitions of SO_2 and HC_3N . Regarding the dust source SMA2, it is unclear whether it harbors a central heating source or is the result of a strong shock. Nonetheless, the masses and locations of SMA1 and SMA2 are broadly consistent with the Mac Low et al. (2007) model of secondary collapse in material swept up in the expanding shells of UCHII regions. Located outside the UCHII shell, we detect a cold dust object (SMA-S) that is remarkably free of line emission. Assuming a low temperature of 15-20K,

we estimate a mass of 12-20 M_{\odot} , which suggests it is likely to be an intermediate mass pre-protostellar core. Beyond SMA-S, we detect the beginning of a filamentary structure of dust and gas emission that extends for several arcseconds eastward before turning northeast. Whether this structure is related in any way to the UCHII region is an open question.

We thank C. Watson for providing access to BIMA data on this region. CJC is supported by a National Science Foundation Graduate Research Fellowship. RI was supported in part during this research by a NASA Spitzer fellowship to UVa. This research has made use of NASA’s Astrophysics Data System Bibliographic Services and the SIMBAD database operated at CDS, Strasbourg, France, and is based in part on observations collected at the European Southern Observatory, Paranal, Chile. This research used the facilities of the Canadian Astronomy Data Centre operated by the National Research Council of Canada with the support of the Canadian Space Agency. TRH thanks K. T. Constantines for introducing him to the power of Matlab.

REFERENCES

- Acord, J. M., Churchwell, E., & Wood, D. O. S. 1998, *ApJ*, 495, L107
- Acord, J. M., Walmsley, C. M., & Churchwell, E. 1997, *ApJ*, 475, 693
- Akeson, R. L., & Carlstrom, J. E. 1996, *ApJ*, 470, 528
- Altenhoff W., Mezger P.G., Wendker H., Westerhout G., 1960, *Veröff. Univ.-Sternwarte Bonn* 59, 48
- Alvarez, C., Feldt, M., Henning, T., Puga, E., Brandner, W., & Stecklum, B. 2004, *ApJS*, 155, 123
- Apai, D., Linz, H., Henning, T., & Stecklum, B. 2005, *A&A*, 434, 987
- Argon, A. L., Reid, M. J., & Menten, K. M. 2003, *ApJ*, 593, 925
- Ball, R., Arens, J. F., Jernigan, J. G., Keto, E., & Meixner, M. M. 1992, *ApJ*, 389, 616
- Beckert, T., Duschl, W. J., & Mezger, P. G. 2000, *A&A*, 356, 1149
- Beltran, M. T., Estalella, R., Girart, J. M., Ho, P. T. P., & Anglada, G. 2007, *ArXiv e-prints*, 712, arXiv:0712.1757

- Beuther, H., Walsh, A. J., Thorwirth, S., Zhang, Q., Hunter, T. R., Megeath, S. T., & Menten, K. M. 2007, *A&A*, 466, 989
- Bik, A., Kaper, L., & Waters, L. B. F. M. 2006, *A&A*, 455, 561
- Brogan, C. L., Hunter, T. R., Indebetouw, R., Chandler, C. J., Shirley, Y. L., Rao, R., & Sarma, A. P. 2007a, *Ap&SS*, 380
- Brogan, C. L., Chandler, C. J., Hunter, T. R., Shirley, Y. L., & Sarma, A. P. 2007b, *ApJ*, 660, L133
- Bronfman, L., Nyman, L.-A., & May, J. 1996, *A&AS*, 115, 81
- Cesaroni, R., Walmsley, C. M., Koempe, C., & Churchwell, E. 1991, *A&A*, 252, 278
- Choi, M., Evans, N. J., II, & Jaffe, D. T. 1993, *ApJ*, 417, 624
- Churchwell, E., Wolfire, M. G., & Wood, D. O. S. 1990, *ApJ*, 354, 247
- Churchwell, E. 2002, *ARA&A*, 40, 27
- Churchwell, E. 1997, *ApJ*, 479, L59
- Comerón, F., Pasquali, A., & Torra, J. 2006, *A&A*, 457, 553
- Comito, C., Schilke, P., Endesfelder, U., Jiménez-Serra, I., & Martín-Pintado, J. 2007, *A&A*, 469, 207
- Cyganowski, C. J., Brogan, C. L., & Hunter, T. R. 2007, *AJ*, 134, 346
- Demircan, O., & Kahraman, G. 1991, *Ap&SS*, 181, 313
- Dickinson, C., Davies, R. D., & Davis, R. J. 2003, *MNRAS*, 341, 369
- Di Francesco, J., Johnstone, D., Kirk, H., MacKenzie, T., & Ledwosinska, E. 2008, *ApJS*, 175, 277
- Doty, S. D., Schöier, F. L., & van Dishoeck, E. F. 2004, *A&A*, 418, 1021
- Eisner, J. A., & Carpenter, J. M. 2006, *ApJ*, 641, 1162
- Faison, M., Churchwell, E., Hofner, P., Hackwell, J., Lynch, D. K., & Russell, R. W. 1998, *ApJ*, 500, 280
- Feldt, M., et al. 2003, *ApJ*, 599, L91

- Feldt, M., Stecklum, B., Henning, T., Launhardt, R., & Hayward, T. L. 1999, *A&A*, 346, 243
- Fish, V. L., Reid, M. J., Argon, A. L., & Zheng, X.-W. 2005, *ApJS*, 160, 220
- Fish, V. L., Reid, M. J., Wilner, D. J., & Churchwell, E. 2003, *ApJ*, 587, 701
- Flower, D. R., Pineau Des Forêts, G., & Walmsley, C. M. 2006, *A&A*, 456, 215
- Frerking, M. A., Langer, W. D., & Wilson, R. W. 1982, *ApJ*, 262, 590
- Genzel, R., & Downes, D. 1977, *A&AS*, 30, 145
- Gomez, Y., Rodriguez, L. F., Garay, G., & Moran, J. M. 1991, *ApJ*, 377, 519
- Hanson, M. M., Luhman, K. L., & Rieke, G. H. 2002, *ApJS*, 138, 35
- Harvey, P. M., & Forveille, T. 1988, *A&A*, 197, L19
- Harvey, P. M., Lester, D. F., Colome, C., Smith, B., Monin, J.-L., & Vauglin, I. 1994, *ApJ*, 433, 187
- Hatchell, J., Thompson, M. A., Millar, T. J., & MacDonald, G. H. 1998, *A&AS*, 133, 29
- Hilditch, R. W., & Bell, S. A. 1987, *MNRAS*, 229, 529
- Hofner, P., & Churchwell, E. 1996, *A&AS*, 120, 283
- Hofner, P., Wyrowski, F., Walmsley, C. M., & Churchwell, E. 2000, *ApJ*, 536, 393
- Hunter, T. R., Churchwell, E., Watson, C., Cox, P., Benford, D. J., & Roelfsema, P. R. 2000, *AJ*, 119, 2711
- Hunter, T. R., Brogan, C. L., Megeath, S. T., Menten, K. M., Beuther, H., & Thorwirth, S. 2006, *ApJ*, 649, 888
- Jørgensen, J. K., Johnstone, D., van Dishoeck, E. F., & Doty, S. D. 2006, *A&A*, 449, 609
- Fuente, A. 2008, *Ap&SS*, 313, 135
- Klaassen, P. D., Plume, R., Ouyed, R., von Benda-Beckmann, A. M., & Di Francesco, J. 2006, *ApJ*, 648, 1079
- Kraemer, K. E., & Jackson, J. M. 1995, *ApJ*, 439, L9
- Kurtz, S., Hofner, P., & Álvarez, C. V. 2004, *ApJS*, 155, 149

- Liljeström, T., & Gwinn, C. R. 2000, *ApJ*, 534, 781
- Mac Low, M.-M., Toraskar, J., Oishi, J. S., & Abel, T. 2007, *ApJ*, 668, 980
- Mangum, J. Shirley, Y. 2006, <https://wikio.nrao.edu/pub/Main/MolInfo/column-density-calculation.pdf>
- Mangum, J. G., & Wootten, A. 1994, *ApJ*, 428, L33
- Martín-Hernández, N. L., Bik, A., Kaper, L., Tielens, A. G. G. M., & Hanson, M. M. 2003, *A&A*, 405, 175
- Mookerjee, B., Casper, E., Mundy, L. G., & Looney, L. W. 2007, *ApJ*, 659, 447
- Neri, R., et al. 2007, *A&A*, 468, L33
- Puga, E., Feldt, M., Alvarez, C., Henning, T., Apai, D., Le Coarer, E., Chalabaev, A., & Stecklum, B. 2006, *ApJ*, 641, 373
- Sandell, G. 1994, *MNRAS*, 271, 75
- Scheuer, P. A. G. 1960, *MNRAS*, 120, 231
- Sollins, P. K., et al. 2004, *ApJ*, 616, L35
- Stark, D. P., Goss, W. M., Churchwell, E., Fish, V. L., & Hoffman, I. M. 2007, *ApJ*, 656, 943
- Thompson, M. A., Hatchell, J., Walsh, A. J., MacDonald, G. H., & Millar, T. J. 2006, *A&A*, 453, 1003
- Thompson, M. A., & MacDonald, G. H. 1999, *A&AS*, 135, 531
- Velázquez, P. F., Dubner, G. M., Goss, W. M., & Green, A. J. 2002, *AJ*, 124, 2145
- Watson, C., Churchwell, E., Zweibel, E. G., & Crutcher, R. M. 2007, *ApJ*, 657, 318
- Watson, A. M., Coil, A. L., Shepherd, D. S., Hofner, P., & Churchwell, E. 1997, *ApJ*, 487, 818
- Wood, D. O. S. 1993, *Massive Stars: Their Lives in the Interstellar Medium*, 35, 108
- Wood, D. O. S., & Churchwell, E. 1989, *ApJS*, 69, 831
- Wright, M. C. H., Plambeck, R. L., & Wilner, D. J. 1996, *ApJ*, 469, 216

Zhang, Q., & Ho, P. T. P. 1995, *ApJ*, 450, L63

Zhang, Q., Hunter, T. R., Sridharan, T. K., & Cesaroni, R. 1999, *ApJ*, 527, L117

Zijlstra, A. A., & Pottasch, S. R. 1988, *A&A*, 196, L9

Zijlstra, A. A., Pottasch, S. R., Engels, D., Roelfsema, P. R., Hekkert, P. T.-L., & Umana, G. 1990, *MNRAS*, 246, 217

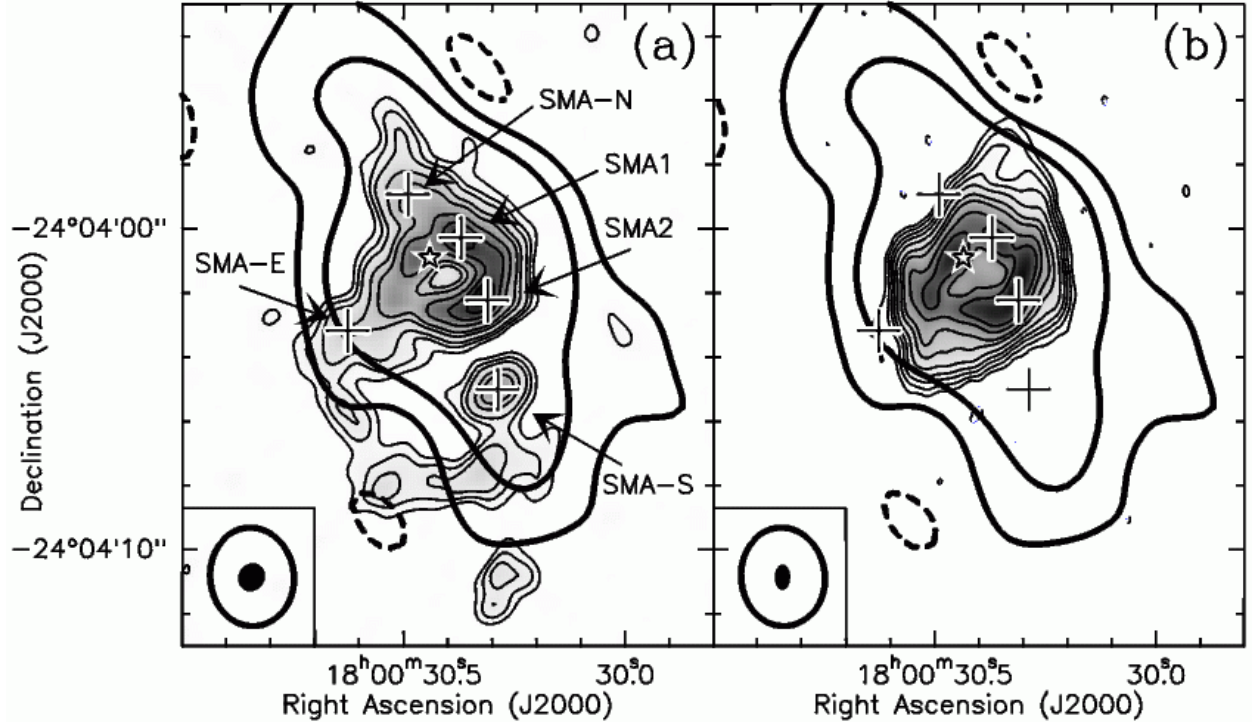


Fig. 1.— (a) Greyscale and thin contours: SMA continuum image at 875 μm with a resolution of $0''.90 \times 0''.79$ at position angle -32° . Contour levels are -20, 20, 39, 65, 130, 195, 325, 455, 585 mJy beam^{-1} . Thick contours: SMA continuum image at 1.4 mm with a resolution of $3''.1 \times 2''.6$ at position angle $+5^\circ$. Contour levels are -50, 50, 250 mJy beam^{-1} . (b) Greyscale and thin contours: VLA 2 cm image with a resolution of $0''.79 \times 0''.47$ at position angle -1° . Contour levels are -0.9, 0.9, 3, 7.5, 15, 30, 60, 90, 150, 210 mJy beam^{-1} . Thick contours: SMA continuum image at 1.4 mm. The respective beams are shown in the lower left corners. The star symbol marks the location of Feldt's star (Feldt et al. 2003). The large crosses denote regions of excess 875 μm emission above that expected from free-free emission extrapolated from cm wavelengths (see Figure 4 and Table 4).

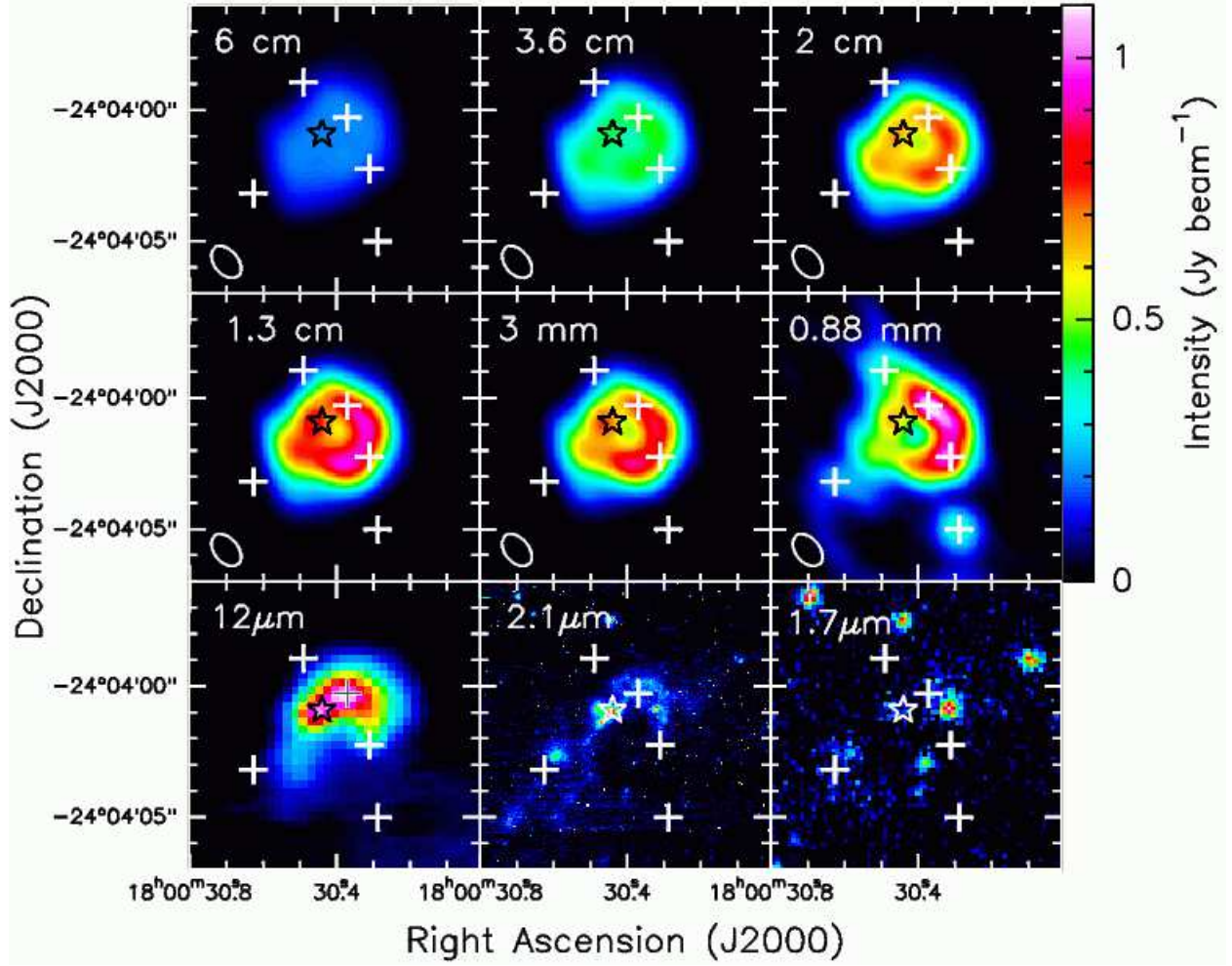


Fig. 2.— Continuum images of G5.89-0.39 from low frequency in the upper left to high frequency in the lower right. The top six images have been restored with the beamsize of the 3 mm image ($1''.40 \times 0''.90$ at P.A.=+35°), and are shown on the same colorscale (0.0 to 1.1 Jy beam⁻¹). The white crosses mark the positions of the submillimeter dust sources identified in Figure 4 and Table 4. The star symbol marks the position of Feldt's star (Feldt et al. 2003).

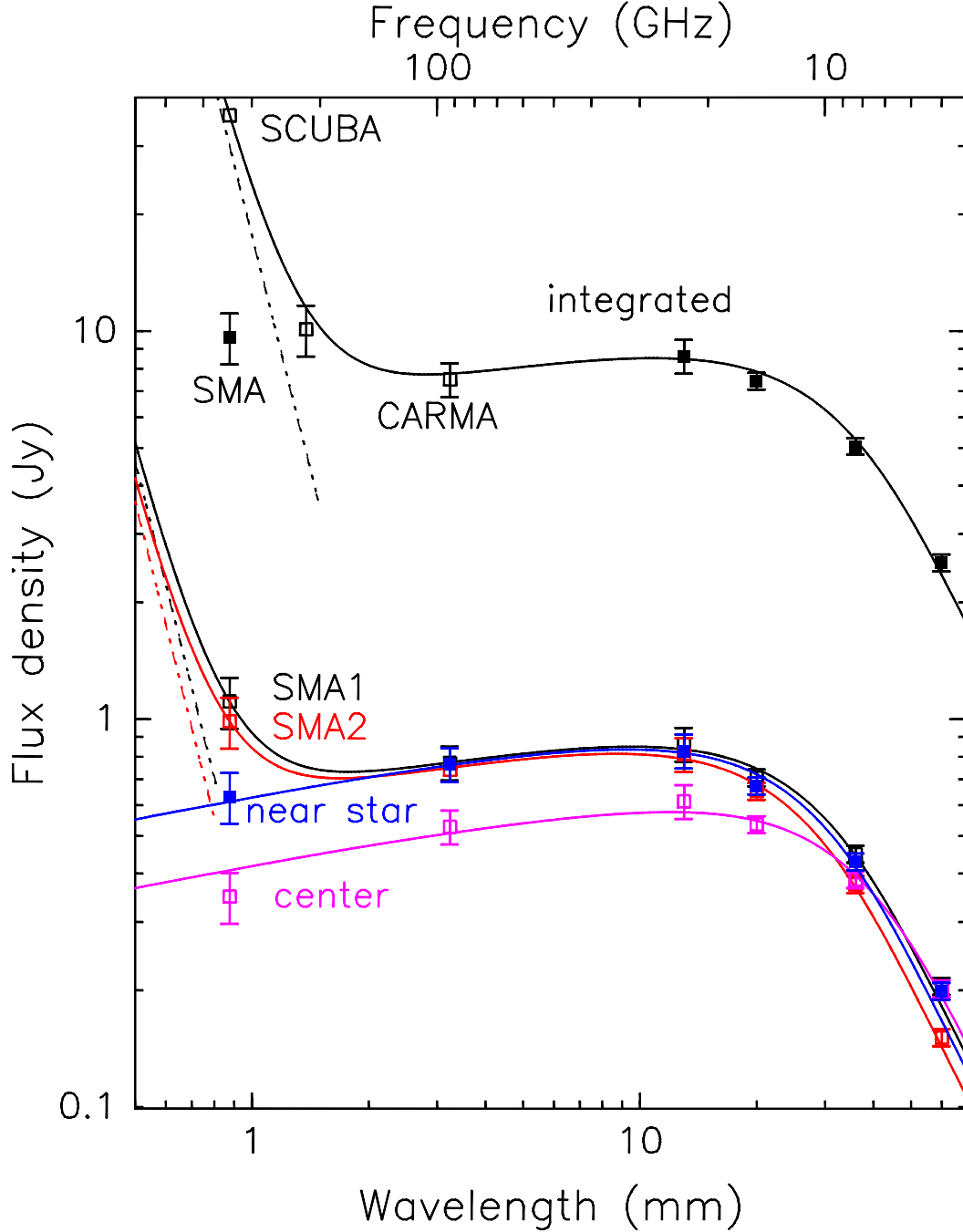


Fig. 3.— Spectral energy distribution at four positions. Lower black line and points: SMA1; red line and points: SMA2; purple line and points: center of shell; blue line and points: $0''.3$ east of Feldt’s star (see Table 3). The upper black line and points are the flux densities integrated over a $12''$ square box. The solid lines are models constructed from free-free emission (Beckert et al. 2000), plus (in the case of SMA1, SMA2 and integrated) dust emission with a ν^4 spectrum, shown as a dash-dot line. The upper open squares are the SCUBA peak flux density and the integrated flux densities from the 1.4 mm SMA data and the 3 mm CARMA data. The error bars reflect the uncertainty values in Table 3.

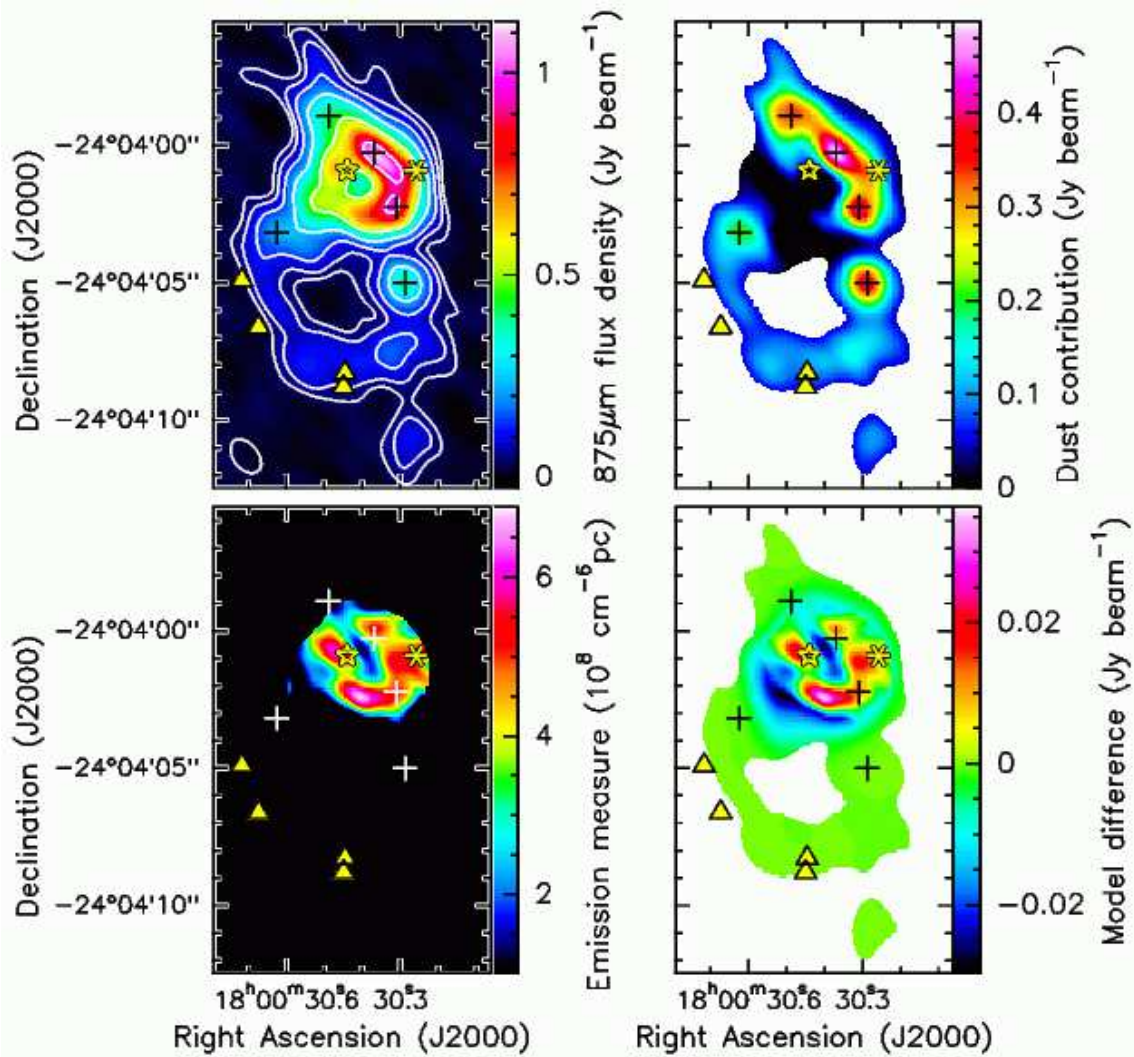


Fig. 4.— *Top left panel:* Observed SMA continuum image at $875\ \mu\text{m}$ restored with a resolution of $1''.40 \times 0''.90$ at position angle $+35^\circ$. The beam is shown in the lower left corner. Contour levels are $-0.03, 0.06, 0.12, 0.24, 0.48, 0.96\ \text{Jy beam}^{-1}$. *Top right panel:* Estimated dust contribution to the observed flux density, computed by scaling the $1.3\ \text{cm}$ image by 0.715 , and removing it from the $875\ \mu\text{m}$ image. The $875\ \mu\text{m}$ image was masked at the $50\ \text{mJy}$ level prior to subtraction. *Bottom left panel:* Model of the emission measure vs. position computed by comparing the flux ratio between the $1.3\ \text{cm}$ and $3\ \text{mm}$ images on a pixel-by-pixel basis. At $1.3\ \text{cm}$, the model has a mean optical depth of 0.115 , and a maximum optical depth of 0.268 . *Bottom right panel:* The difference between the dust image shown in the top right panel and the dust image produced by using the free-free model shown in the bottom left panel. In all panels, the star symbol marks the location of Feldt's star, and the black crosses denote the positions of sources of dust emission (see Table 4). The triangles mark near-IR H_2 emission components (A, D1, D2), and the yellow asterisk is the $\text{Br}\gamma$ outflow origin, all from Puga et al. (2006).

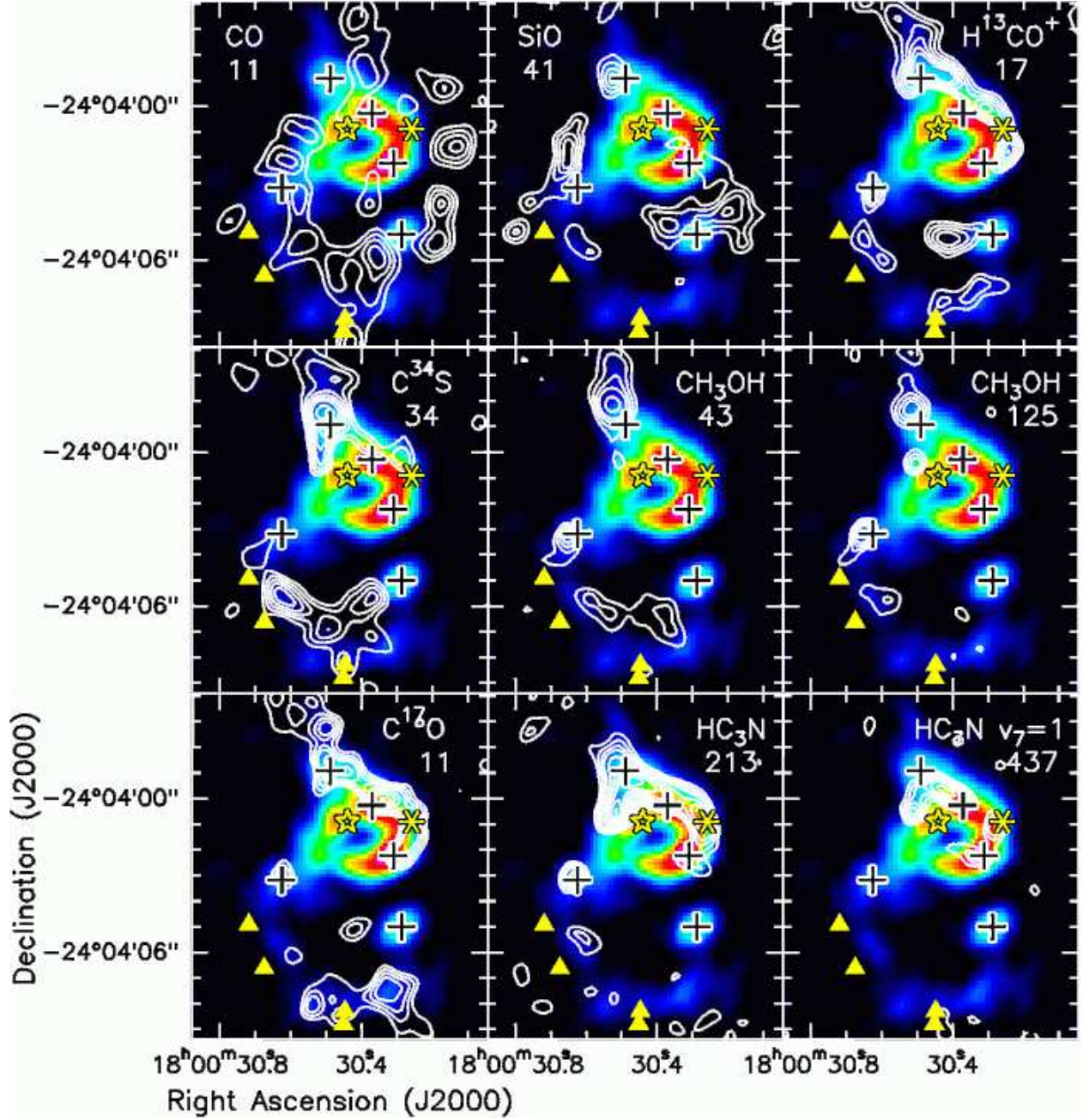


Fig. 5.— Integrated intensity contour maps of submillimeter spectral lines overlaid on the SMA 875 μm continuum image. The black crosses mark the positions of the dust sources SMA1, SMA2, SMA-N, SMA-E, and SMA-S (see Table 4). The yellow triangles mark the near-IR H_2 knots (A, D1, D2), and the yellow asterisk marks the origin of the $\text{Br}\gamma$ outflow (Puga et al. 2006). Contour levels are 3, 4, 5, 6, 7, 8, 10, 12, 14, 16, 18, 20 \times the base level listed in Table 5. The number below the species name is the energy above ground for the lower level in units of cm^{-1} . The image for HC_3N is the average image of the two lines in the table. The image for $\text{HC}_3\text{N } v_7 = 1$ is the average image of the three lines in the table.

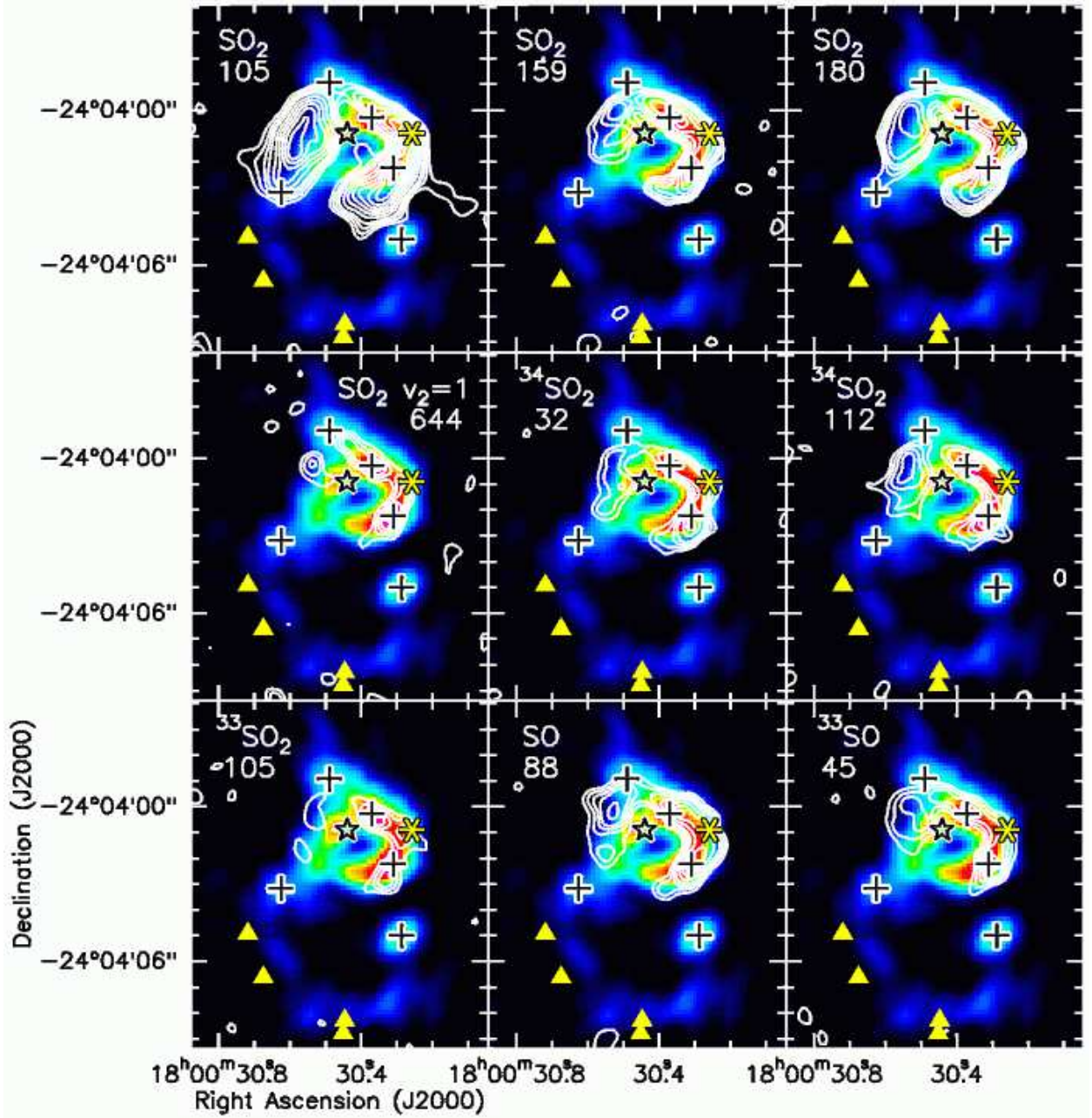


Fig. 6.— Integrated intensity contour maps of submillimeter SO and SO₂ spectral lines overlaid on the SMA 875 μ m continuum image. The black crosses mark the positions of the dust sources SMA1, SMA2, SMA-N, SMA-E, and SMA-S (see Table 4). The yellow triangles mark the near-IR H₂ knots (A, D1, D2), and the yellow asterisk marks the origin of the Br γ outflow (Puga et al. 2006). Contour levels are 3, 4, 5, 6, 7, 8, 10, 12, 14, 16, 18, 20 \times the base level listed in Table 5. The number below the species name is the energy above ground for the lower level in units of cm⁻¹. The image for SO₂ $v_2 = 1$ is the average image of the two lines in the table.

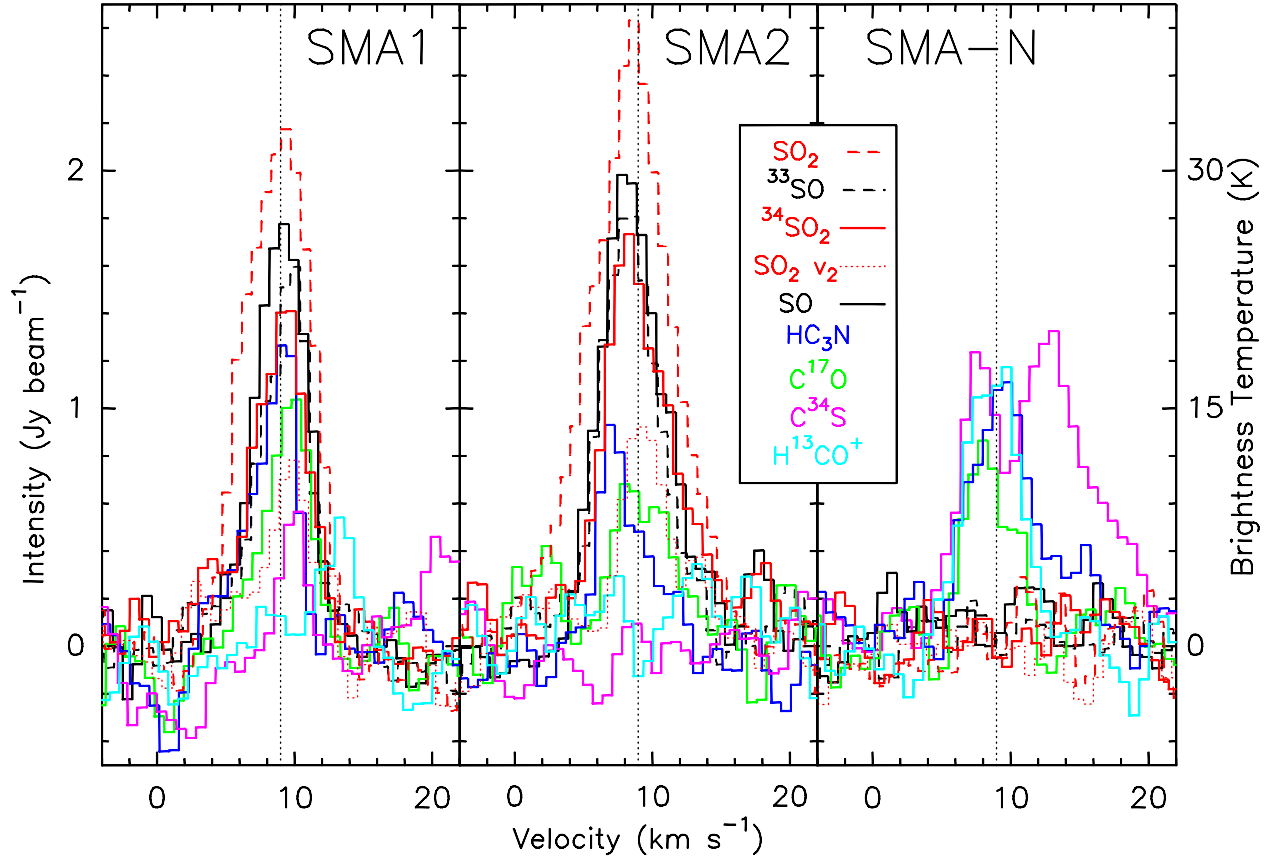


Fig. 7.— Spectral line profiles extracted from a single data cube pixel at the positions of the dust continuum sources SMA1, SMA2, and SMA-N. The dotted vertical line marks the LSR velocity of $+9 \text{ km s}^{-1}$. The SO_2 line is $16_{7,9} - 17_{6,12}$, the $^{34}\text{SO}_2$ line is $17_{4,14} - 17_{3,15}$, the HC_3N line is $38-37$, and the CH_3OH line is $7_{1,7,+0} - 6_{1,6,+0}$.

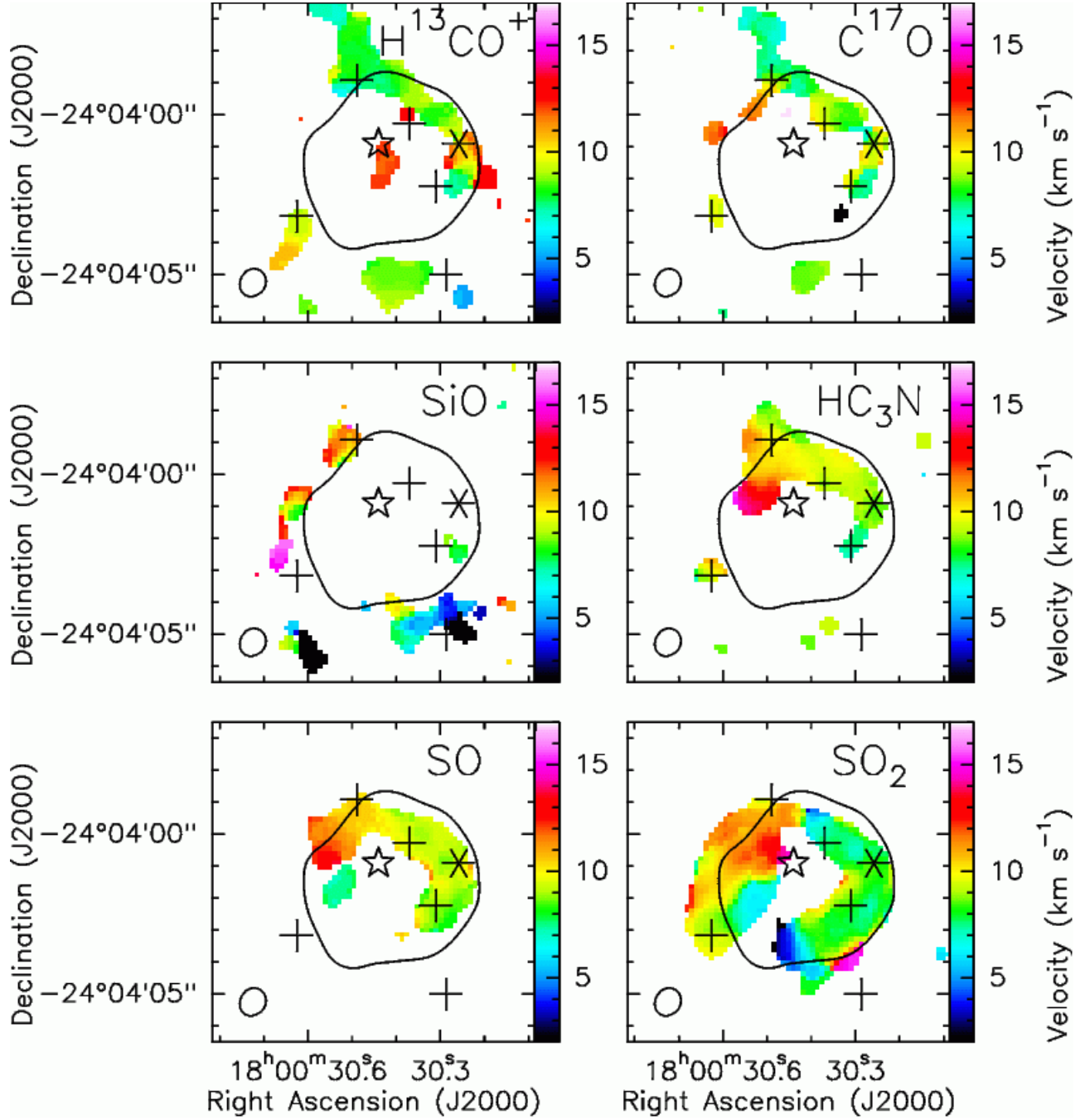


Fig. 8.— Plotted in color scale are the first moment maps of various transitions from the 875 μm SMA dataset. The black contour is from the 3 mm CARMA continuum image (0.1 Jy beam^{-1}). The crosses mark the dust sources from Table 4 and the asterisk marks the origin of the $\text{Br}\gamma$ outflow (Puga et al. 2006). The star symbol marks the position of Feldt's star (Feldt et al. 2003). The SMA beam ($0''.90 \times 0''.79$ at P.A. $=-32^\circ$) is drawn at the lower left.

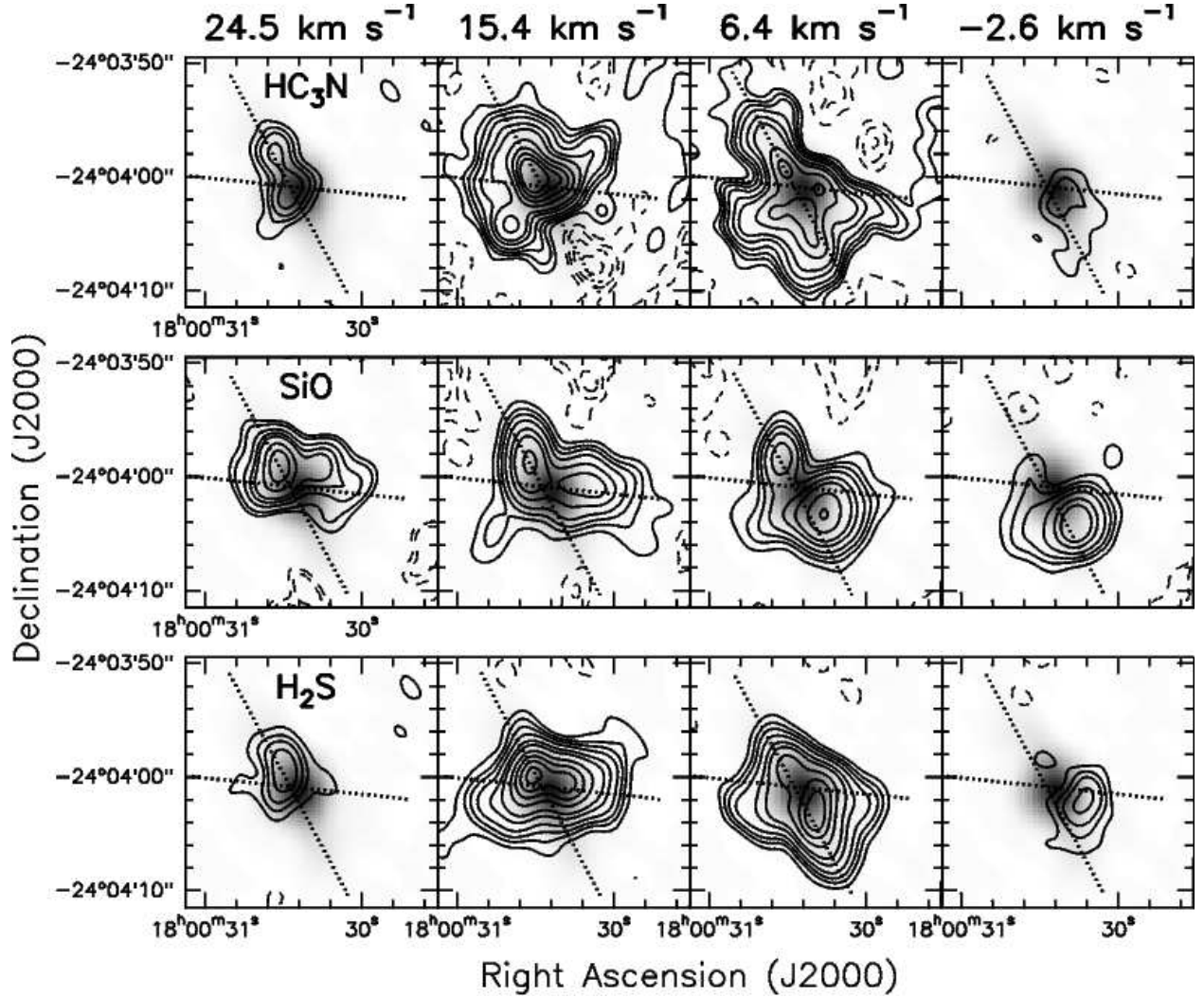


Fig. 9.— Contour channel maps of three spectral lines from the 1.4 mm SMA dataset: HC_3N 25-24, SiO 5-4, and H_2S $2_{2,0} - 2_{1,1}$, observed with a beamsize of $3''.1 \times 2''.6$ at P.A. $= +5^\circ$. Each panel is comprised of eight channels of width 1.1 km s^{-1} centered at the velocity listed; there are no gaps in velocity coverage between panels. Contour levels are $-7, -5, -3, 3, 5, 7, 10, 15, 20, 30, 40, 50, 60 \times 0.6 \text{ Jy beam}^{-1} \text{ km s}^{-1}$ for HC_3N , $\times 1.2 \text{ Jy beam}^{-1} \text{ km s}^{-1}$ for SiO , and $\times 0.55 \text{ Jy beam}^{-1} \text{ km s}^{-1}$ for H_2S . In each panel, the greyscale image is the 217 GHz continuum, and the dotted lines mark the position angles reported (counter-clockwise from north) in SiO (5-4) (Sollins et al. 2004) and CO (1-0) (Watson et al. 2007). The position angle of the single-dish CO (3-2) outflow (Klaassen et al. 2006) is similar to that shown for CO (1-0).

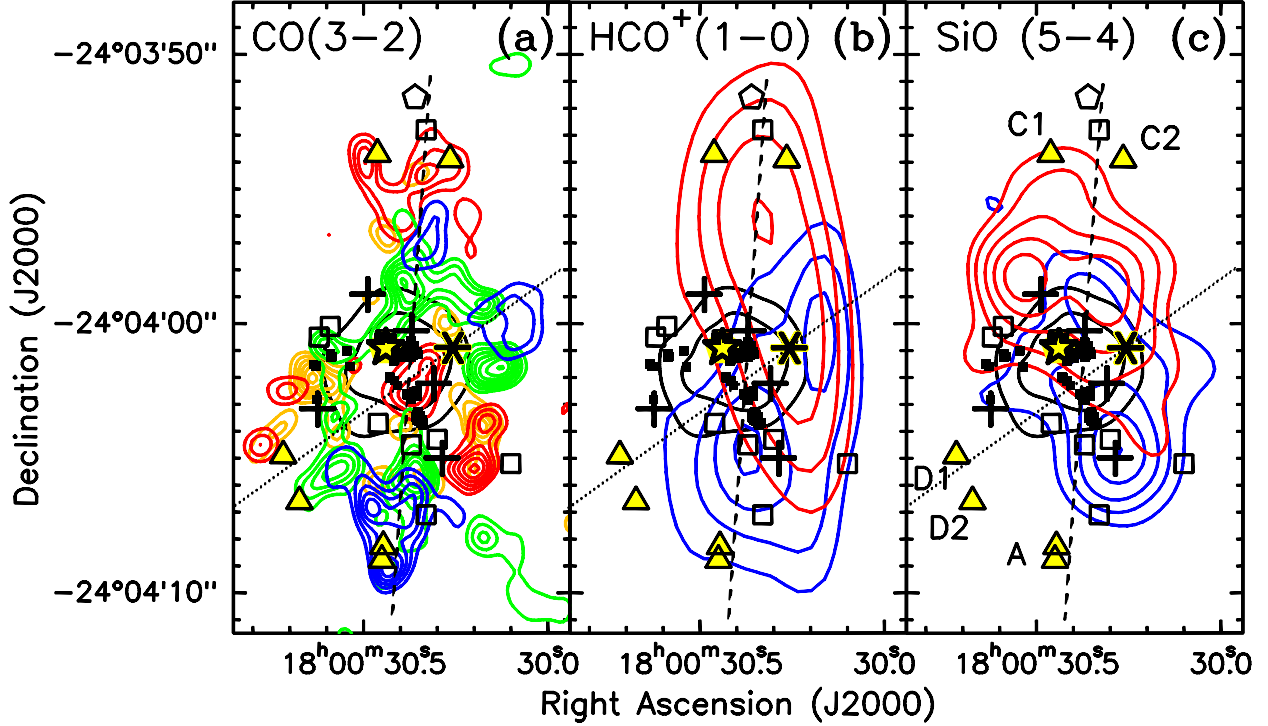


Fig. 10.— (a) Contour map of CO (3-2) emission observed with a beamsize of $0''.88 \times 0''.77$ with P.A. $=-37^\circ$. The velocity ranges of integration are $+80$ to $+40$ km s^{-1} (red contours), $+40$ to $+20$ km s^{-1} (orange), -4 to -41 km s^{-1} (green), -41 to -81 km s^{-1} (blue). The contour levels are 15, 20, 25, 30, 37.5, 45, 52.5, 60, 67.5 $\text{Jy beam}^{-1} \text{ km s}^{-1}$. (b) Contour map of the high velocity HCO^+ (1-0) emission from the dataset of Watson et al. (2007) with a beamsize of $8''.5 \times 3''.5$ (P.A. $= 1.4^\circ$); red contours: $+30$ to $+55$ km s^{-1} with levels 4.5, 6.3, 8.1, 9.9 $\text{Jy beam}^{-1} \text{ km s}^{-1}$; blue contours: -20 to -45 km s^{-1} with levels 2, 2.75, 3.5, 4.25 $\text{Jy beam}^{-1} \text{ km s}^{-1}$. (c) Contour map of the high velocity SiO (5-4) emission from the Sollins et al. (2004) data with a beamsize of $3''.1 \times 2''.6$ at P.A. $=+5^\circ$, and identical velocity ranges as for HCO^+ . Levels are 4, 7, 10, 14, 18 $\text{Jy beam}^{-1} \text{ km s}^{-1}$. In all panels, the black contours are from the 3 mm continuum image (0.1 and 0.5 Jy beam^{-1}). Filled squares are OH masers from Stark et al. (2007), open squares are H_2O masers from Hofner & Churchwell (1996), triangles are the near-IR H_2 knots from Puga et al. (2006), and the pentagon is a Class I CH_3OH maser position (component 2 from Kurtz et al. (2004)). The dashed line indicates the outflow axis associated with the dust source SMA1 while the dotted line represents the orientation of the $\text{Br}\gamma$ outflow and the asterisk marks it origin (Puga et al. 2006).

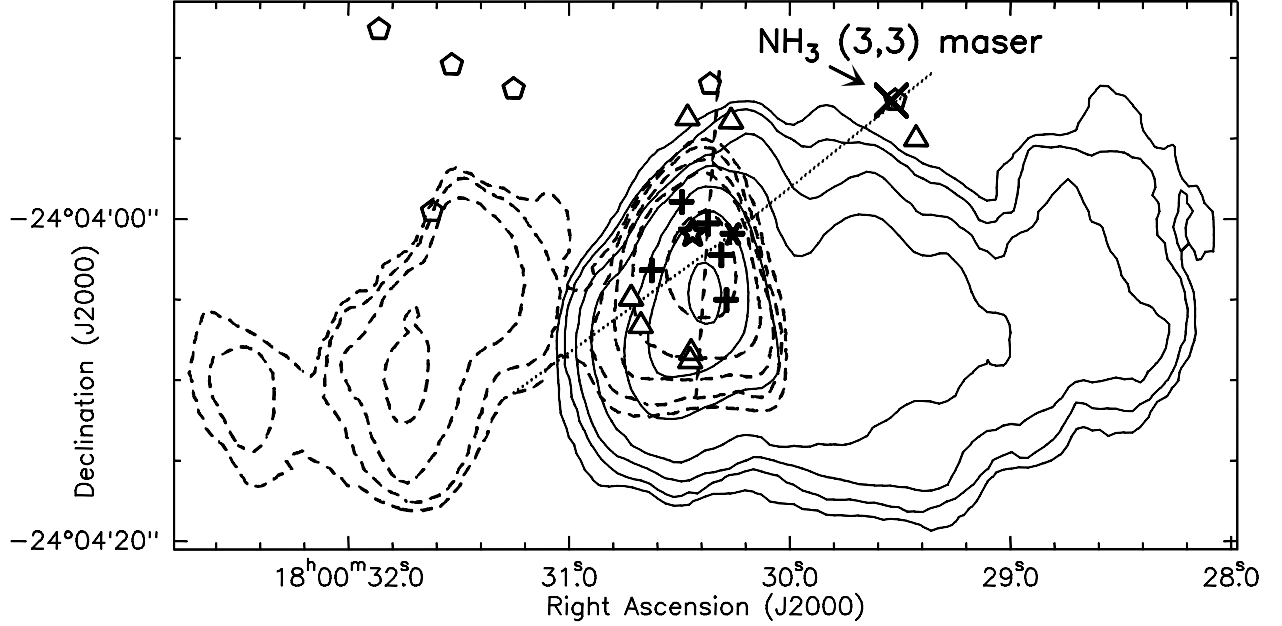


Fig. 11.— Contour maps of CO (1-0) emission from the dataset of Watson et al. (2007) observed with a beamsize of $7''.7 \times 3''.5$ with P.A.= $+1^\circ$. The velocity ranges of integration are $+20$ to $+58$ km s⁻¹ (dashed contours), and 0 to -37 km s⁻¹ (solid contours). These ranges begin at slightly higher velocities and extend to higher velocities than those shown in Watson et al. (2007). Levels are 5, 10, 20, 40, 80, 160 Jy beam⁻¹ km s⁻¹. Triangles are the near-IR H₂ knots from Puga et al. (2006), pentagons are Class I CH₃OH masers from Kurtz et al. (2004), crosses are the 875 μm dust sources, and the “X” is the NH₃ (3,3) maser from this work. The dashed line indicates the outflow axis associated with the dust source SMA1 while the dotted line represents the orientation of the Brγ outflow source (asterisk) (Puga et al. 2006).

Table 1: Summary of VLA archival data

Project Code	Date YYYY-MM-DD	Freq. (GHz)	Wave. (cm)	Observation Type	Config.	Continuum sensitivity (mJy beam ⁻¹)	Beam " × " (P.A.)	Calibrators
AW158 ^a	1986-04-27	5	6.0	continuum	A	1.3	0''.85 × 0''.43 (-17°)	3C286, J1748-253
AA227	1998-06-24	8.4	3.6	continuum	BnA	0.17	0''.60 × 0''.45 (+73°)	3C286, J1730-130
AW550	2001-05-12	15	2.0	recomb. line	B	0.30	0''.79 × 0''.47 (-1°)	J2251+158
AZ075	1995-11-17	22	1.3	NH ₃ (2,2), (3,3)	B	1.8 ^b	0''.73 × 0''.32 (+22°)	3C286, J1730-130

^a Data originally published by Wood & Churchwell (1989).

^b Line free channels from both IFs combined.

Table 2. ESO Archival Infrared Images

telescope	instrument	filter/band	observation date	program	PI
VLT-Yepun	NACO	H ₂ 2.122μm	2004/06/15	073.C-0178(A)	Feldt
VLT-Yepun	NACO	Brγ 2.166μm	2004/06/15	073.C-0178(A)	Feldt
VLT-Yepun	NACO	L' 3.8μm	2004/06/15	073.C-0178(A)	Feldt
VLT-Yepun	NACO	K _s 2.1μm	2004/06/15	073.C-0178(A)	Feldt
NTT	SOFI	Brγ	1999/08/01	63.H-0292(A)	Kaper
NTT	SOFI	Brγ-continuum	1999/08/01	63.H-0292(A)	Kaper
NTT	SOFI	1.215μm	1999/08/01	63.H-0292(A)	Kaper
VLT-Antu	ISAAC	1.71μm	2002/07/09	69.C-0448(A)	Bik
3.6m	TIMMI2	11.9μm	2003/07/20	71.C-0342(A)	Brooks

Table 3: Comparative continuum intensities at various positions in the UCHII region

Position	Flux density (Jy beam ⁻¹) ^a					
	6 cm	3.6 cm	2 cm	1.3 cm	3 mm	875 μm
SMA1	0.205	0.449	0.706	0.863	0.771	1.11
SMA2	0.151	0.375	0.652	0.812	0.740	0.987
center of shell ^b	0.202	0.386	0.535	0.614	0.528	0.349
0''.3 east of Feldt's star ^c	0.199	0.429	0.673	0.829	0.765	0.632
total (within a 12'' box)	2.36	4.93	7.37	8.81	7.51	6.44
calibration uncertainty	5%	5%	5%	10%	10%	15%

^aAll images have been restored to the beamsize of the 3 mm image: 1''.40 × 0''.90 at P.A. = +35°.

^bJ2000 position: 18:00:30.402, -24:04:01.39

^cJ2000 position: 18:00:30.463, -24:04:00.97

Table 4: 875 μm positions and flux densities of dust sources

Source	Position		Peak flux	Peak brightness	Integrated
	α (h m s)	δ ($^{\circ}$ ' ")	density ^a Jy beam ⁻¹	temperature K	flux density ^{a,b} Jy
SMA1	18 00 30.37	-24 04 00.27	0.50	4.2	0.50 ± 0.08^c
SMA2	18 00 30.30	-24 04 02.37	0.40	3.3	0.40 ± 0.06^c
SMA-N	18 00 30.48	-24 03 58.87	0.31	2.6	0.74 ± 0.11
SMA-S	18 00 30.29	-24 04 05.03	0.38	3.2	0.52 ± 0.09
SMA-E	18 00 30.62	-24 04 03.14	0.19	1.6	0.45 ± 0.08

^avalues taken from the free-free subtracted image with resolution of $1''.40 \times 0''.90$

^buncertainties include the 15% calibration uncertainty

^csource is unresolved

Table 5: Spectral lines detected in the 875 μm SMA data

Species	Transition	Frequency (GHz)	Sideband	E_{lower} (cm^{-1})	Base contour $\text{Jy beam}^{-1} \text{ km s}^{-1}$
CH_3OH	$7_{1,7,+0} - 6_{1,6,+0}$	335.58200	lower	43.7	4.02
SO_2	$23_{3,21} - 23_{2,22}$	336.08923	lower	180.6	3.76
HC_3N	37-36	336.52008	lower	202.1	2.40
SO	$11_{10} - 10_{10}$	336.55381	lower	88.1	2.87
SO_2	$16_{7,9} - 17_{6,12}$	336.66958	lower	159.1	2.76
CH_3OH	$12_{1,11,-0} - 12_{0,12,+0}$	336.86511	lower	125.7	3.55
C^{17}O	3-2	337.06113 ^b	lower	11.2	1.65
^{33}SO	$8_{7,9} - 7_{6,8}$	337.19862	lower	44.7	3.73
$\text{HC}_3\text{N } v_7 = 1$	$37_1 - 36_{-1}$	337.34469	lower	425.6	0.90
C^{34}S	7-6	337.39646	lower	33.8	4.46
$^{34}\text{SO}_2$	$7_{4,4} - 7_{3,5}$	345.51966	upper	32.7	3.30
$^{34}\text{SO}_2$	$6_{4,2} - 6_{3,3}$	345.55309	upper	28.2	..
$^{33}\text{SO}_2$	$19_{1,19} - 18_{0,18}$	345.58500 ^a	upper	105.1	2.81
HC_3N	38-37	345.60901	upper	213.3	..
$^{34}\text{SO}_2$	$5_{4,2} - 5_{3,3}$	345.65129	upper	24.4	.. ^c
$^{34}\text{SO}_2$	$4_{4,0} - 4_{3,1}$	345.67879	upper	21.1	.. ^c
^{12}CO	3-2	345.79599	upper	11.5	41.4
CH_3OH	$16_{1,15} - 15_{2,14}$	345.90397	upper	219.7	.. ^c
CH_3OH	$18_{-3,16} - 17_{-4,14}$	345.91919	upper	307.8	.. ^c
$^{34}\text{SO}_2$	$17_{4,14} - 17_{3,15}$	345.92935	upper	112.5	3.26
CH_3OH	$5_{4,2} - 6_{3,3}$	346.20278	upper	68.5	.. ^c
NS	$8_{1,-1,9} - 7_{1,1,8}$	346.22014	upper	37.8	.. ^c
$\text{HC}_3\text{N } v_7 = 1$	$38_{-1} - 37_1$	346.45573	upper	436.8	..
SO_2	$16_{4,12} - 16_{3,13}$	346.52388	upper	102.7	.. ^c
SO	$8_9 - 7_8$	346.52848	upper	43.2	.. ^c
$\text{SO}_2 v_2 = 1$	$18_{4,14} - 18_{3,15}$	346.59179	upper	643.6	1.62
SO_2	$19_{1,19} - 18_{0,18}$	346.65217	upper	105.3	5.16
$\text{HC}_3\text{N } v_7 = 1$	$38_1 - 37_{-1}$	346.94912	upper	437.1	-
H^{13}CO^+	4-3	346.99834	upper	17.4	3.10
SiO	8-7	347.33056	upper	40.6	5.77

^acomprised of 4 hyperfine components

^bcomprised of 14 components

^cblended with adjacent lines

Table 6: Results of Gaussian fits of lines toward SMA1 and SMA2

Species	E_{lower} (cm^{-1})	Amplitude ^a (Jy beam ⁻¹)	SMA1		Amplitude ^a (Jy beam ⁻¹)	SMA2	
			Velocity (km s ⁻¹)	FWHM (km s ⁻¹)		Velocity (km s ⁻¹)	FWHM (km s ⁻¹)
³⁴ SO ₂	32.7	1.38 ± 0.06	9.06 ± 0.11	5.27 ± 0.28	1.69 ± 0.08	8.64 ± 0.13	6.08 ± 0.34
³³ SO ₂	105.1	1.03 ± 0.06	9.32 ± 0.14	4.92 ± 0.35	1.06 ± 0.06	8.82 ± 0.11	4.18 ± 0.27
HC ₃ N	213	1.17 ± 0.10	8.95 ± 0.17	3.96 ± 0.42	0.83 ± 0.06	8.08 ± 0.17	4.77 ± 0.45
³⁴ SO ₂	112.5	1.32 ± 0.06	9.30 ± 0.11	4.83 ± 0.26	1.51 ± 0.06	9.12 ± 0.12	5.80 ± 0.30
SO ₂	105.3	2.06 ± 0.06	7.76 ± 0.09	5.96 ± 0.22	4.33 ± 0.06	8.08 ± 0.06	7.94 ± 0.14
SO ₂	180.6	2.28 ± 0.06	8.44 ± 0.07	5.69 ± 0.17	2.36 ± 0.05	8.13 ± 0.07	7.22 ± 0.17
HC ₃ N	202.1	1.06 ± 0.09	9.03 ± 0.17	4.00 ± 0.42	0.90 ± 0.05	8.51 ± 0.10	3.47 ± 0.25
SO	88.1	1.81 ± 0.05	9.43 ± 0.06	4.42 ± 0.15	1.91 ± 0.06	8.78 ± 0.08	5.37 ± 0.20
SO ₂	159.1	1.67 ± 0.05	8.59 ± 0.08	5.38 ± 0.20	2.08 ± 0.07	8.17 ± 0.10	5.90 ± 0.25
C ¹⁷ O	11.2	1.05 ± 0.07	9.18 ± 0.13	3.99 ± 0.32	0.59 ± 0.08	8.82 ± 0.29	4.54 ± 0.71
³³ SO	44.7	1.48 ± 0.07	9.76 ± 0.09	4.10 ± 0.21	1.74 ± 0.06	8.66 ± 0.08	4.80 ± 0.19
weighted average			8.94 ± 0.03	4.94 ± 0.07		8.42 ± 0.03	6.07 ± 0.07

^aThe conversion from flux density to brightness temperature is approximately 15.0 K/Jy in both sidebands.

Table 7: Gas masses from C¹⁷O (3-2)

Source Name	Integrated		$T_{\text{exc}} = 75$ K		$T_{\text{exc}} = 150$ K		
	Intensity ^a (Jy km s ⁻¹)	$\tau_{\text{C}^{17}\text{O}(3-2)}$ (neper)	N(C ¹⁷ O) log(cm ⁻²)	H ₂ mass ^b (M _⊙)	$\tau_{\text{C}^{17}\text{O}(3-2)}$ (neper)	N(C ¹⁷ O) log(cm ⁻²)	H ₂ mass ^b (M _⊙)
SMA1	4.1 ± 0.8	0.24	12.79	1.1 ± 0.3	0.11	12.97	1.6 ± 0.4
SMA2	3.6 ± 0.7	0.13	12.70	0.9 ± 0.3	0.06	12.89	1.4 ± 0.3

^aMeasured at the positions in Table 4; includes absolute calibration uncertainty

^bAssuming the abundance ratio of C¹⁷O to H₂ to be 4.8×10^{-8}